Harmonic Linearization and Investigation of Three-Phase Parallel-Structured Signal Decomposition Algorithms in Grid-Connected Applications

Saeed Golestan, *Senior Member, IEEE*, Josep M. Guerrero, *Fellow, IEEE*, Juan C. Vasquez, *Senior Member, IEEE*, Abdullah M. Abusorrah, *Senior Member, IEEE*, and Yusuf Al-Turki, *Senior Member, IEEE*

***Abstract*—In practice, because of different factors, the supply voltage (especially in the distribution level) almost always has some degrees of imbalance and harmonic pollution. With increasing the level of these power quality issues in recent years, their monitoring and compensation using custom power devices have received much attention. In addition, modern power converter based renewable energy sources are expected to provide some ancillary services to mitigate these power quality issues. These tasks and requirements often involve using a signal processing tool for the online detection of the fundamental sequence components and harmonics of the voltage and/or current signals. The typical choice for this purpose is the discrete Fourier transform as it offers a fast computational speed. It, however, may not be a very attractive solution for applications where the selective extraction of a few frequency components is required as it demands a high computational effort. In such scenarios, using time-domain signal decomposition algorithms is more desirable. Generally speaking, these algorithms are nonlinear feedback control systems, which include two or more dynamically interactive frequency-adaptive filters tuned to concerned frequency components. The complex structure of these algorithms, however, makes them complicated to analyze, especially for those who are not experienced in this field. This article aims to address this difficulty by developing harmonic models for these algorithms and investigating them. To this end, three case studies are considered. Through a harmonic linearization procedure, developing harmonic models for them is shown. The accuracy of these models is then investigated, and performing the harmonic stability analysis using them is demonstrated.**

Manuscript received May 10, 2020; revised July 10, 2020; accepted August 11, 2020. Date of publication September 4, 2020; date of current version November 20, 2020. This work was supported in part by the Deanship of Scientific Research, King Abdulaziz University, Jeddah, under Grant RG-12-135-39 and in part by VILLUM FONDEN under the VILLUM Investigator Grant (25920): Center for Research on Microgrids. Recommended for publication by Associate Editor C. N. M. Ho. *(Corresponding author: Saeed Golestan.)*

Saeed Golestan, Josep M. Guerrero, and Juan C. Vasquez are with the Department of Energy Technology, Aalborg University, DK-9220 Aalborg, Denmark (e-mail: sgd@et.aau.dk; joz@et.aau.dk; juq@et.aau.dk).

Abdullah M. Abusorrah and Yusuf Al-Turki are with the Department of Electrical and Computer Engineering, Faculty of Engineering and the Center of Research Excellence in Renewable Energy and Power Systems, King Abdulaziz University, Jeddah 21481, Saudi Arabia (e-mail: aabusorrah@kau.edu.sa; yaturki@yahoo.com).

Color versions of one or more of the figures in this article are available online at https://ieeexplore.ieee.org.

Digital Object Identifier 10.1109/TPEL.2020.3021723

***Index Terms*—Frequency-locked loop (FLL), harmonics, phase-locked loop (PLL), reduced-order generalized integrator (ROGI), second-order generalized integrator (SOGI), signal decomposition, synchronization, three-phase systems, voltage imbalance.**

I. Introduction

A THREE-PHASE supply voltage is balanced if all signals have the same magnitude with 120° phase difference compared to each other. In practice, however, a completely balanced supply voltage may not be reached. In fact, because of different factors, such as supplying single-phase and/or unbalanced three-phase loads, asymmetry in the line impedance and/or transformer windings, and occurring faults, the supply voltage may have some degrees of imbalance [1]. In addition to the phase and amplitude imbalance, the nonfundamental current (the harmonic current) drawn by nonlinear loads may cause some deformities in the supply voltage. This is especially true in the distribution level, where the current drawn by some nonlinear loads is far away from a sine wave [2].

The presence of harmonics in the supply voltage and its phase/amplitude imbalance may have adverse effects on the efficiency and lifetime of the equipment and may even jeopardize the power system stability. For example, it is known that the imbalance of the voltage supplying three-phase induction motors, which consume around 70% of industrial electricity, results in an oscillating electromagnetic force [1]. Such an oscillating force increases vibrations and losses in induction motors and, hence, reduces their efficiency and lifetime. The grid voltage imbalance may also cause an uncontrolled negative-sequence current flow into grid-tied power converters and, therefore, generate uncontrolled double-frequency oscillations in their output power and dc-link voltage [3]. Such oscillations may give rise to a system trip and, consequently, the loss of generation and even instability. Regarding the presence of harmonics in the supply voltage, these disturbances may lead to extra losses in conductors of both neutral and line and also in the winding and core of transformers and cause resonance in the power system [4].

To deal with the ever-increasing problems associated with harmonics and imbalance in the supply voltage, monitoring and compensation of these disturbances using custom power devices have received a considerable attention [5], [6]. In addition, power converter interfaced renewable energy generation systems, which their penetration in power systems is significantly increasing, are expected to have some additional control functions to deal with these power quality issues and provide some ancillary services to support the power grid in the presence of them [3], [7]–[10]. In wind farms, for example, the national and international grid codes [11], [12] demand power converter interfaced wind turbines to have a fault ride-through capability to support the power grid during faults, which are almost always unbalanced. In microgrids, as another example, power converters are expected to have the harmonic and negative sequence current sharing capability in addition to the standard active/reactive power sharing ability to ensure proper operation under unbalanced and/or harmonically distorted grid conditions [10]. All these requirements and functions often involve an online detection of the fundamental symmetrical components and/or harmonics of the voltage and/or current signals [3], [13].

The typical choice for the extraction of harmonics and sequence components is computing the discrete Fourier transform (DFT) using a fast Fourier transform (FFT) algorithm [2], [14], [15]. From the computing speed point of view, the FFT has a fast response as it only requires one cycle of the sampled data. It means that extracting the harmonic content of a 50-Hz signal only takes 0.02 s. Besides, the FFT does not require the knowledge of expected harmonics. The accuracy of the FFT, however, may be considerably affected under frequency drifts and nonstationary situations. In addition, it is a computationally demanding algorithm as it calculates all harmonics within the signal bandwidth. The DFT and its close variants are subsumed under the category of frequency-domain methods [2], [14].

In a large number of applications, especially in microgrid and renewable energy areas, only extracting the fundamental symmetrical components and/or a few low-order harmonics are often required, and quite large frequency drifts are expected. In such scenarios, time-domain approaches are more cost-effective solutions than frequency-domain ones from the computational point of view.

The theory of symmetrical components [16] plays a key role in designing time-domain signal decomposition algorithms. According to this theory, an unbalanced set of three-phase signals is decomposable into three sets of signals called the positive, negative, and zero sequence components. Such a decomposition involves generating 120° phase-shifted versions of the three-phase signals, which can be translated into a 90° shift for facilitating its practical implementation [17]. The way of generating this 90° phase shift is the key difference between the algorithms that work based on the theory of symmetrical components. Using generalized integrators and enhanced phase-locked loop (PLL) are probably two of the most popular approaches for this purpose [17]–[21]. It is worth mentioning here that for applications where the zero sequence component is not required, the procedure for extracting the positive- and negative sequence components can be further simplified by transferring the three-phase signals to the $\alpha\beta$ frame by applying Clarke's transformation.[1]

Using complex-coefficient filters (CCFs) are also highly popular for detecting and separating harmonics and fundamental sequence components of three-phase signals in the time domain. A CCF, which is characterized by having an asymmetrical frequency response around zero Hertz and, therefore, a sequence-selective filtering ability, is often realized by creating couplings between two orthogonal axes in the $\alpha\beta$ frame [22], [23]. Using the concept of the synchronous reference frame PLL (SRF-PLL), which has been proven to be an adaptive complex filter [24], is an alternative way [25].

Overall, it may be said that time-domain signal decomposition algorithms, regardless of their design concept, are adaptive nonlinear feedback control systems that are widely employed in the control system of grid-tied power converters and custom power devices. As these algorithms may significantly affect the stability and performance of this equipment, ensuring their robustness and stable operation is of paramount importance. This task, however, is not trivial at all because of the nonlinear nature and interactive elements of these algorithms. The traditional solution to deal with this challenge is developing linear time-invariant (LTI) models for them. Such a solution, however, may not be practical here as the main instability cause in these algorithms is dynamic interactions between their parallel-connected frequency-adaptive elements, but developing an LTI model involves neglecting them. To deal with this problem, the harmonic linearization[2] of time-domain signal decomposition algorithms and developing linear time-periodic (LTP) models for them are presented in this article. The LTP model, contrary to the LTI one, can take into account the presence of harmonics and/or imbalance in the input of time-domain signal decomposition algorithms and also the dynamic interactions between their elements. Therefore, it can be a very efficient and reliable tool for the stability and dynamics assessment of these algorithms.

This article focuses on the LTP modeling and investigation of three-phase parallel-structured signal decomposition algorithms and makes the following contributions to the field.

1) To demonstrate the procedure for developing LTP models for different time-domain signal decomposition algorithms, three case studies, namely, the dual reduced-order generalized integrator based frequency-locked loop (DROGI-FLL) [26]–[30], dual second-order generalized integrator based FLL (DSOGI-FLL) [19], and modified universal three-phase signal processor (UTSP) [25] are considered, and their LTP models are derived using a detailed mathematical procedure. To ensure the accuracy of these models, extensive numerical results are presented.
2) The procedure for obtaining the harmonic transfer function (HTF) of a signal decomposition algorithm from its LTP model is presented, its stability assessment using its HTF is discussed, and the effect of control parameters on its stability is theoretically analyzed and numerically verified.

[1] Clarke's transformation eliminates the zero sequence component.

[2] The harmonic linearization means the linearization around a periodic trajectory, which is determined according to the number and frequency of concerned disturbance components.

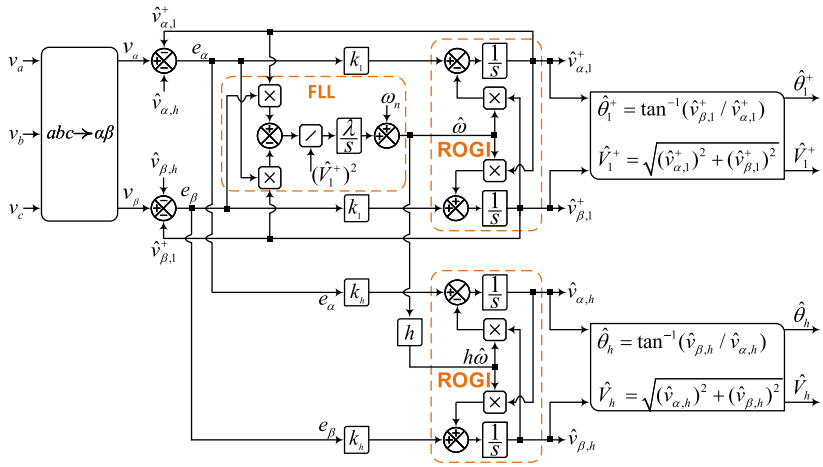

Fig. 1. DROGI-FLL. k_1, k_h, and λ are the control gains. $\hat{v}_{\alpha,1}^+$ and $\hat{v}_{\beta,1}^+$ ($\hat{v}_{\alpha,h}$ and $\hat{v}_{\beta,h}$) are estimations of the FFPS (h-order frequency) component of the grid voltage in the $\alpha\beta$ frame. $\hat{\theta}_1^+$ and $\hat{V}_1^+$ ($\hat{\theta}_h$ and $\hat{V}_h$) are the estimation of the phase angle and amplitude of the FFPS (h-order frequency) component of the grid voltage. $\hat{\omega}$ is an estimation of the fundamental angular frequency of the grid voltage. $\omega_n = 2\pi 50$ rad/s.

3) It is demonstrated that the case studies of this article, despite having completely different structures, have very close relationships together. It means that the observations and conclusions made for one case are valid for other cases.

II. Dual Reduced-Order Generalized Integrator Based FLL

A. Overview

A complex signal, which is a mathematical concept, is a set of two signals in two distinct paths at a moment in time, where their couplings are described by a complex operator j. In this way, signal processing and filter design become more compact and insightful. The complex signal processing and filter design have a long history of use in different engineering applications. For example, in grid-connected applications, designing complex filters dates back to around two decades ago [31], [32].

In the power and energy area, a basic building block in designing complex filters is often a complex integrator [33], also known as the reduced-order generalized integrator (ROGI) [34]. The ROGI is described in the Laplace domain as

$$G_{\mathrm{ROGI}}(s) = \frac{1}{s - j\omega_c} \tag{1}$$

where ω_c is the ROGI's center frequency.

In designing signal decomposition algorithms, which this article focuses on, a parallel connection of multiple ROGIs tuned to concerned frequency components is often recommended [26]–[30]. Adapting the ROGIs center frequency to grid frequency changes is often carried out using a frequency observer, which is called FLL. The interested reader can find more details in this regard in [26]–[30].

In its simplest possible form, a ROGI-based signal decomposition algorithm includes two parallel ROGIs (centered at the fundamental positive frequency and an h-order disturbance frequency) and an FLL for adapting their center frequencies to frequency changes. This structure, which is referred to as the DROGI-FLL (see Fig. 1), is considered as the first case study in this article. The DROGI-FLL can extract the fundamental-frequency positive sequence (FFPS) component, an h-order frequency component, and their phase, frequency, and amplitude. The following should be mentioned.

1) h in the DROGI-FLL in Fig. 1 can be a positive or negative integer. A negative value means that extracting a frequency component of the negative sequence is required.
2) $h = -1$ means that extracting the fundamental-frequency negative sequence (FFNS) component is intended.
3) By adding additional ROGIs tuned to concerned harmonic frequencies, one can easily extend the DROGI-FLL for extracting an arbitrary number of components. In this case, the resulting structure should be called the multiple ROGI-FLL.

B. Harmonic Modeling

1) Assumptions: It is assumed that the three-phase input signal of the DROGI-FLL includes the FFPS component and an h-order frequency component, which is as follows:

$$\overbrace{\begin{pmatrix} v_a \\ v_b \\ v_c \end{pmatrix}}^{\boldsymbol{v}_{abc}} = \overbrace{\begin{pmatrix} V_1^+ \cos(\theta_1^+) \\ V_1^+ \cos(\theta_1^+ - 2\pi/3) \\ V_1^+ \cos(\theta_1^+ + 2\pi/3) \end{pmatrix}}^{\boldsymbol{v}^+_{abc,1}} + \overbrace{\begin{pmatrix} V_h \cos(\theta_h) \\ V_h \cos(\theta_h - 2\pi/3) \\ V_h \cos(\theta_h + 2\pi/3) \end{pmatrix}}^{\boldsymbol{v}_{abc,h}} \tag{2}$$

where V_1^+ and θ_1^+ (V_h and θ_h) denote the amplitude and phase angle of the FFPS (the h-order frequency) component, respectively, and h is a nonzero integer. Note that depending

on the sign of h, the h-order component can be of positive or negative sequence. Note also that considering or neglecting a zero sequence component in (2) does not cause any difference as Clarke's transformation in the input of the DROGI-FLL blocks it.

Transferring (2) to the $\alpha\beta$ frame gives

$$\overbrace{\begin{pmatrix} v_\alpha \\ v_\beta \end{pmatrix}}^{\boldsymbol{v}_{\alpha\beta}} = \overbrace{\begin{pmatrix} V_1^+ \cos(\theta_1^+) \\ V_1^+ \sin(\theta_1^+) \end{pmatrix}}^{\boldsymbol{v}^+_{\alpha\beta,1}} + \overbrace{\begin{pmatrix} V_h \cos(\theta_h) \\ V_h \sin(\theta_h) \end{pmatrix}}^{\boldsymbol{v}_{\alpha\beta,h}}. \tag{3}$$

Considering (3), it can be concluded that the extracted FFPS and h-order frequency component by the DROGI-FLL should be of the form

$$\begin{pmatrix} \hat{v}^+_{\alpha,1} \\ \hat{v}^+_{\beta,1} \end{pmatrix} = \begin{pmatrix} \hat{V}_1^+ \cos(\hat{\theta}_1^+) \\ \hat{V}_1^+ \sin(\hat{\theta}_1^+) \end{pmatrix}, \quad \begin{pmatrix} \hat{v}_{\alpha,h} \\ \hat{v}_{\beta,h} \end{pmatrix} = \begin{pmatrix} \hat{V}_h \cos(\hat{\theta}_h) \\ \hat{V}_h \sin(\hat{\theta}_h) \end{pmatrix}. \tag{4}$$

The actual parameters V_1^+, θ_1^+, V_h, and θ_h in (3) and their estimations in (4) are defined as a nominal value (indicated by the subscript n) plus a small perturbation (indicated by Δ), which are as follows:

$$\begin{aligned} V_1^+ &= V_{n,1}^+ + \Delta V_1^+, & \hat{V}_1^+ &= V_{n,1}^+ + \Delta \hat{V}_1^+ \\ \theta_1^+ &= \theta_{n,1}^+ + \Delta\theta_1^+, & \hat{\theta}_1^+ &= \theta_{n,1}^+ + \Delta\hat{\theta}_1^+ \\ V_h &= V_{n,h} + \Delta V_h, & \hat{V}_h &= V_{n,h} + \Delta \hat{V}_h \\ \theta_h &= \theta_{n,h} + \Delta\theta_h, & \hat{\theta}_h &= \theta_{n,h} + \Delta\hat{\theta}_h \end{aligned} \tag{5}$$

where $\theta_{n,1}^+ = \omega_n t$ and $\theta_{n,h} = h\omega_n t + \delta_h$.

The grid fundamental angular frequency and its estimation are also defined as

$$\begin{aligned} \omega &= \omega_n + \Delta\omega \\ \hat{\omega} &= \omega_n + \Delta\hat{\omega} \end{aligned} \tag{6}$$

where $\omega_n = 2\pi 50$ rad/s.

Throughout this article, it is assumed that the actual and estimated parameters are approximately equal, which implies that small-signal perturbations are only considered.

2) Harmonic Linearization: From Fig. 1, we have

$$\hat{V}_1^+ = \sqrt{(\hat{v}^+_{\alpha,1})^2 + (\hat{v}^+_{\beta,1})^2} \Rightarrow \frac{d\hat{V}_1^+}{dt} = \frac{\hat{v}^+_{\alpha,1}\frac{d\hat{v}^+_{\alpha,1}}{dt} + \hat{v}^+_{\beta,1}\frac{d\hat{v}^+_{\beta,1}}{dt}}{\hat{V}_1^+} \tag{7a}$$

$$\hat{\theta}_1^+ = \tan^{-1}\left(\frac{\hat{v}^+_{\beta,1}}{\hat{v}^+_{\alpha,1}}\right) \Rightarrow \frac{d\hat{\theta}_1^+}{dt} = \frac{\hat{v}^+_{\alpha,1}\frac{d\hat{v}^+_{\beta,1}}{dt} - \hat{v}^+_{\beta,1}\frac{d\hat{v}^+_{\alpha,1}}{dt}}{(\hat{V}_1^+)^2} \tag{7b}$$

$$\hat{V}_h = \sqrt{(\hat{v}_{\alpha,h})^2 + (\hat{v}_{\beta,h})^2} \Rightarrow \frac{d\hat{V}_h}{dt} = \frac{\hat{v}_{\alpha,h}\frac{d\hat{v}_{\alpha,h}}{dt} + \hat{v}_{\beta,h}\frac{d\hat{v}_{\beta,h}}{dt}}{\hat{V}_h} \tag{7c}$$

$$\hat{\theta}_h = \tan^{-1}\left(\frac{\hat{v}_{\beta,h}}{\hat{v}_{\alpha,h}}\right) \Rightarrow \frac{d\hat{\theta}_h}{dt} = \frac{\hat{v}_{\alpha,h}\frac{d\hat{v}_{\beta,h}}{dt} - \hat{v}_{\beta,h}\frac{d\hat{v}_{\alpha,h}}{dt}}{(\hat{V}_h)^2} \tag{7d}$$

$$\frac{d\hat{\omega}}{dt} = \lambda \frac{\overbrace{(v_\beta - \hat{v}^+_{\beta,1} - \hat{v}_{\beta,h})}^{e_\beta}\hat{v}^+_{\alpha,1} - \overbrace{(v_\alpha - \hat{v}^+_{\alpha,1} - \hat{v}_{\alpha,h})}^{e_\alpha}\hat{v}^+_{\beta,1}}{(\hat{V}_1^+)^2} \tag{7e}$$

where

$$\frac{d\hat{v}^+_{\alpha,1}}{dt} = k_1 e_\alpha - \hat{\omega}\hat{v}^+_{\beta,1} \tag{8a}$$

$$\frac{d\hat{v}^+_{\beta,1}}{dt} = k_1 e_\beta + \hat{\omega}\hat{v}^+_{\alpha,1} \tag{8b}$$

$$\frac{d\hat{v}_{\alpha,h}}{dt} = k_h e_\alpha - h\hat{\omega}\hat{v}_{\beta,h} \tag{8c}$$

$$\frac{d\hat{v}_{\beta,h}}{dt} = k_h e_\beta + h\hat{\omega}\hat{v}_{\alpha,h}. \tag{8d}$$

Substituting (8) into (7) results in

$$\frac{d\hat{V}_1^+}{dt} = \frac{k_1}{\hat{V}_1^+}\left[\hat{v}^+_{\alpha,1}e_\alpha + \hat{v}^+_{\beta,1}e_\beta\right] \tag{9a}$$

$$\frac{d\hat{\theta}_1^+}{dt} = \hat{\omega} + \frac{k_1}{(\hat{V}_1^+)^2}\left[-\hat{v}^+_{\beta,1}e_\alpha + \hat{v}^+_{\alpha,1}e_\beta\right] \tag{9b}$$

$$\frac{d\hat{V}_h}{dt} = \frac{k_h}{\hat{V}_h}\left[\hat{v}_{\alpha,h}e_\alpha + \hat{v}_{\beta,h}e_\beta\right] \tag{9c}$$

$$\frac{d\hat{\theta}_h}{dt} = h\hat{\omega} + \frac{k_h}{(\hat{V}_h)^2}\left[-\hat{v}_{\beta,h}e_\alpha + \hat{v}_{\alpha,h}e_\beta\right] \tag{9d}$$

$$\frac{d\hat{\omega}}{dt} = \frac{\lambda}{(\hat{V}_1^+)^2}\left[-\hat{v}^+_{\beta,1}e_\alpha + \hat{v}^+_{\alpha,1}e_\beta\right]. \tag{9e}$$

Considering (3) and (4), (9) can be rewritten as

$$\begin{aligned} \frac{d\hat{V}_1^+}{dt} = k_1\Big[&V_1^+\cos(\theta_1^+ - \hat{\theta}_1^+) - \hat{V}_1^+ + V_h\cos(\theta_h - \hat{\theta}_1^+) \\ &- \hat{V}_h\cos(\hat{\theta}_h - \hat{\theta}_1^+)\Big] \end{aligned} \tag{10a}$$

$$\begin{aligned} \frac{d\hat{\theta}_1^+}{dt} = \hat{\omega} + \frac{k_1}{\hat{V}_1^+}\Big[&V_1^+\sin(\theta_1^+ - \hat{\theta}_1^+) + V_h\sin(\theta_h - \hat{\theta}_1^+) \\ &- \hat{V}_h\sin(\hat{\theta}_h - \hat{\theta}_1^+)\Big] \end{aligned} \tag{10b}$$

$$\begin{aligned} \frac{d\hat{V}_h}{dt} = k_h\Big[&V_h\cos(\theta_h - \hat{\theta}_h) - \hat{V}_h + V_1^+\cos(\theta_1^+ - \hat{\theta}_h) \\ &- \hat{V}_1^+\cos(\hat{\theta}_1^+ - \hat{\theta}_h)\Big] \end{aligned} \tag{10c}$$

$$\begin{aligned} \frac{d\hat{\theta}_h}{dt} = h\hat{\omega} + \frac{k_h}{\hat{V}_h}\Big[&V_h\sin(\theta_h - \hat{\theta}_h) + V_1^+\sin(\theta_1^+ - \hat{\theta}_h) \\ &- \hat{V}_1^+\sin(\hat{\theta}_1^+ - \hat{\theta}_h)\Big] \end{aligned} \tag{10d}$$

$$\begin{aligned} \frac{d\hat{\omega}}{dt} = \frac{\lambda}{\hat{V}_1^+}\Big[&V_1^+\sin(\theta_1^+ - \hat{\theta}_1^+) + V_h\sin(\theta_h - \hat{\theta}_1^+) \\ &- \hat{V}_h\sin(\hat{\theta}_h - \hat{\theta}_1^+)\Big] \end{aligned} \tag{10e}$$

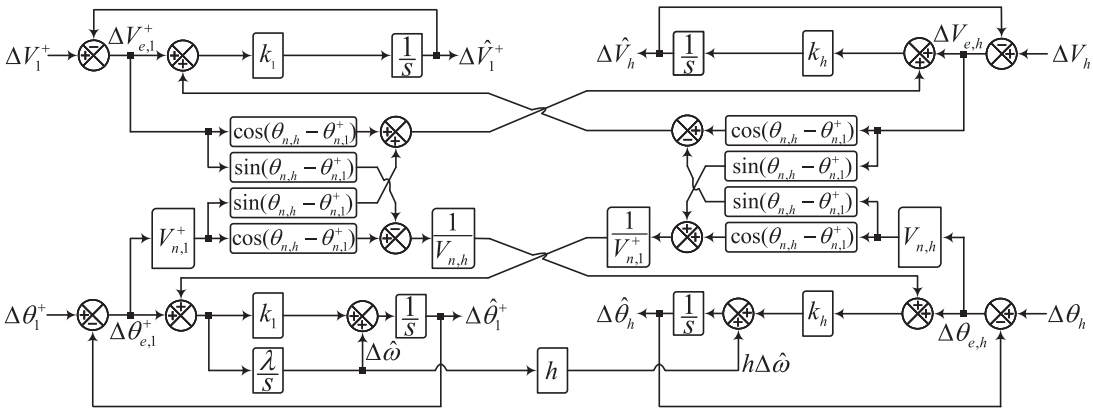

Fig. 2. Harmonic model (LTP model) of the DROGI-FLL.

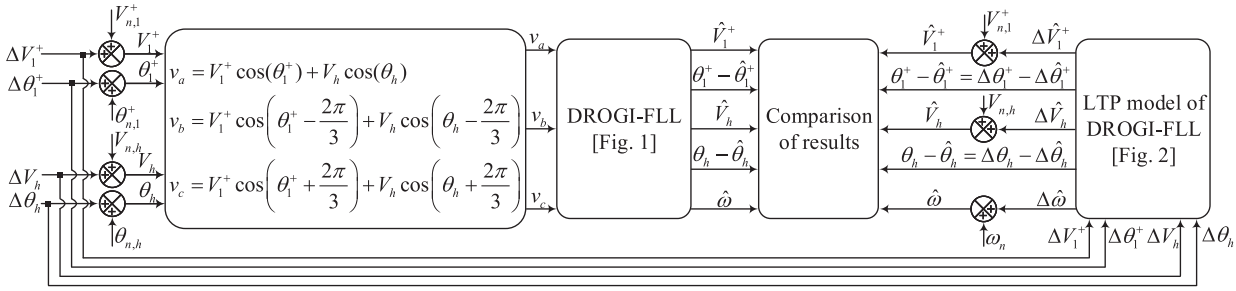

Fig. 3. Schematic diagram of the procedure for the model verification.

which is the set of governing nonlinear differential equations of the DROGI-FLL. Considering the definitions made in (5) and applying trigonometric identities, (10a) can be approximated by (11a). Following a similar procedure, it can be shown that (10b)–(10e) can be approximated by (11b)–(11e), respectively. Details of obtaining (11b)–(11e) are not presented to save space. Using (11a)–(11e), the harmonic model (also called the LTP model) of the DROGI-FLL can be derived, as depicted in Fig. 2. Notice that the harmonic model involves division by $V_{n,1}^+$ and $V_{n,h}$. Therefore, these nominal values cannot be equal to zero.

C. Investigation

1) Model Verification: To investigate the accuracy of the derived harmonic model for the DROGI-FLL, a model verification is conducted. The schematic diagram of the model verification procedure can be observed in Fig. 3.

Two case studies are considered, which are as follows.

1) *Case 1*: The three-phase input signal contains the FFPS and FFNS components. It is corresponding to consider $h = -1$ in the derived harmonic model. The nominal amplitude of the FFPS and FFNS components are 1 and 0.2 p.u., respectively.
2) *Case 2*: The three-phase input signal contains the FFPS component and the seventh harmonic of the positive sequence. It is corresponding to consider $h = +7$ in the derived harmonic model. The nominal amplitude of the FFPS component and the harmonic component is 1 and 0.2 p.u., respectively.

TABLE I
CONTROL PARAMETERS

	Control parameters
DROGI-FLL	$k_1 = k_h = 177$, $\lambda = 16000$
DSOGI-FLL	$k = k_1/(0.5\omega_n) = 1.13$, $\lambda = 16000$
Modified UTSP	$\mu_1 = \mu_2 = 177$, $\mu_3 = 16000$

In each case study, three tests are performed, which are as follows.

1) *Test A*: The magnitude of the FFPS component drops from 1 to 0.9 p.u. at $t = 0.01$ s.
2) *Test B*: The grid frequency undergoes a step change from 50 to 50.5 Hz at $t = 0.01$ s.
3) *Test C*: The magnitude of the disturbance component (i.e., the FFNS component in Case 1 and the harmonic of order $h = +7$ in Case 2) drops from 0.2 to 0.1 p.u. at $t = 0.01$ s.

The control parameters of the DROGI-FLL in both cases are summarized in Table I. The sampling frequency is fixed at 10 kHz. The method suggested in [34, Fig. 7] is used for the discretization of the DROGI-FLL.

Figs. 4 and 5 show the model verification results for Cases 1 and 2, respectively. In both cases, the harmonic model demonstrates a good accuracy in predicting the dynamics of the

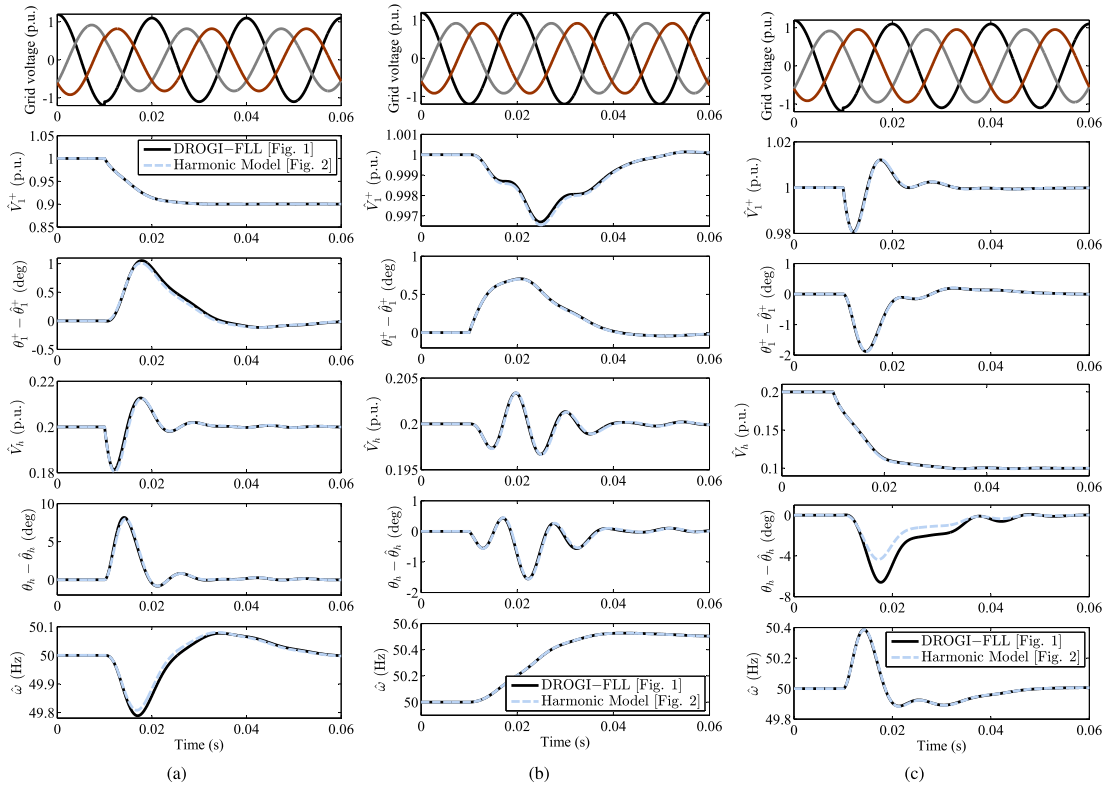

Fig. 4. DROGI-FLL model verification for Case 1. (a) Test A. (b) Test B. (c) Test C.

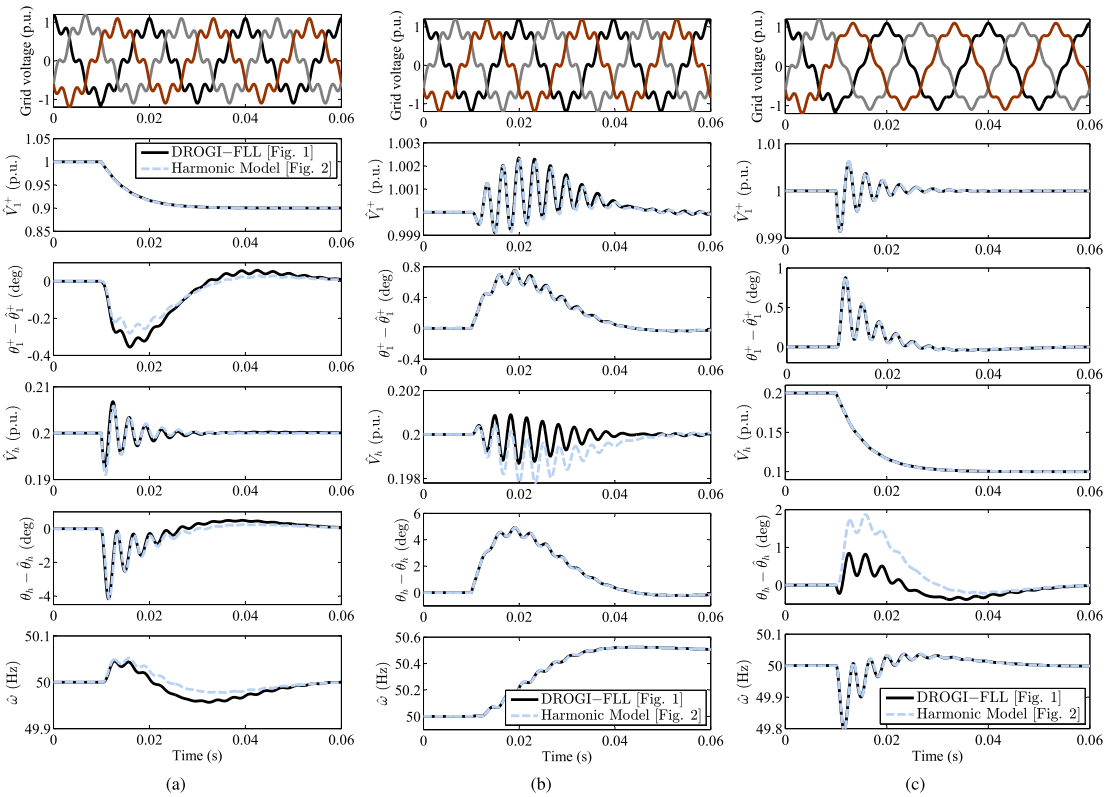

Fig. 5. DROGI-FLL model verification for Case 2. (a) Test A. (b) Test B. (c) Test C.

DROGI-FLL in estimating the FFPS component and the concerned disturbance component and also the dynamic coupling between them. The prediction errors of the harmonic model, which are small, are the result of linearizing nonlinear terms.

2) Harmonic Stability Analysis: Using the harmonic model in Fig. 2, which is obtained based on (11a)–(11e) shown at the bottom of the page, the stability of the DROGI-FLL can be investigated. To this end, the sine and cosine terms in Fig. 2 can be expressed as

$$\cos(\theta_{n,h}-\theta^+_{n,1})=\frac{e^{j\delta_h}e^{j\omega_p t}+e^{-j\delta_h}e^{-j\omega_p t}}{2}$$
$$\sin(\theta_{n,h}-\theta^+_{n,1})=\frac{e^{j\delta_h}e^{j\omega_p t}-e^{-j\delta_h}e^{-j\omega_p t}}{2j} \tag{12}$$

where $\omega_p=(h-1)\omega_n$.

By assuming $\delta_h=0$[3] and substituting (12) into (11a)–(11e) and defining the amplitude and phase error terms in these equations as (13), one may obtain (14) shown at the bottom of the next page by taking the Laplace transform of these equations

$$\Delta V^+_{e,1}=\Delta V^+_1-\Delta\hat{V}^+_1$$
$$\Delta\theta^+_{e,1}=\Delta\theta^+_1-\Delta\hat{\theta}^+_1$$
$$\Delta V_{e,h}=\Delta V_h-\Delta\hat{V}_h$$

[3]This assumption is just for obtaining a more compact open-loop HTF for the DROGI-FLL. Obtaining the open-loop HTF for the case that $\delta_h\neq 0$ may also be carried out easily.

$$\Delta\theta_{e,h}=\Delta\theta_h-\Delta\hat{\theta}_h. \tag{13}$$

Notice that R and Γ in (14) are the ratios of control parameters, i.e., $R=k_h/k_1$ and $\Gamma=\lambda/k_1$.

The matrix equation (14), which is of infinite dimension, is the open-loop HTF of the DROGI-FLL. The stability of the DROGI-FLL can be investigated by using a truncated version of this HTF. For instance, for determining the stability margin of the DROGI-FLL, one may obtain the eigenloci of its open-loop HTF for s belonging to a strip defined by $-j\omega_p/2<\mathrm{Im}(s)<j\omega_p/2$ and determine its phase margin and gain margin in a similar manner as single-input-single-output systems [20], [35], [36]. Fig. 6, which shows the open-loop eigenloci of the DROGI-FLL for the same two cases considered for the model verification in Section II-C.1, makes this fact more clear. Fig. 6 also demonstrates that the frequency of the selected disturbance component has a noticeable effect on the DROGI-FLL stability margin. Recall that the DROGI-FLL uses the same values of the control parameters in both cases. Recall also that the disturbance components in both cases (i.e., the FFNS component in Case 1 and the seventh harmonic of the positive sequence component in Case 2) have the same nominal magnitude.

The stability region of the DROGI-FLL and the effect of control parameters on it may also be determined by applying the generalized Nyquist stability criterion to its open-loop HTP [20], [35], [36]. For example, the predicted stability region for the DROGI-FLL for $h=-1$ and three different values of

$$\frac{d(\Delta\hat{V}^+_1)}{dt}=k_1\Bigg[\overbrace{(V^+_{n,1}+\Delta V^+_1)\cos(\Delta\theta^+_1-\Delta\hat{\theta}^+_1)-(V^+_{n,1}+\Delta\hat{V}^+_1)}^{\approx(\Delta V^+_1-\Delta\hat{V}^+_1)}$$
$$+\cos(\theta_{n,h}-\theta^+_{n,1})\overbrace{\Big\{(V_{n,h}+\Delta V_h)\cos(\Delta\theta_h-\Delta\hat{\theta}^+_1)-(V_{n,h}+\Delta\hat{V}_h)\cos(\Delta\hat{\theta}_h-\Delta\hat{\theta}^+_1)\Big\}}^{\approx(\Delta V_h-\Delta\hat{V}_h)}$$
$$-\sin(\theta_{n,h}-\theta^+_{n,1})\overbrace{\Big\{(V_{n,h}+\Delta V_h)\sin(\Delta\theta_h-\Delta\hat{\theta}^+_1)-(V_{n,h}+\Delta\hat{V}_h)\sin(\Delta\hat{\theta}_h-\Delta\hat{\theta}^+_1)\Big\}}^{\approx V_{n,h}(\Delta\theta_h-\Delta\hat{\theta}_h)}\Bigg]$$
$$\approx k_1\Big[(\Delta V^+_1-\Delta\hat{V}^+_1)+(\Delta V_h-\Delta\hat{V}_h)\cos(\theta_{n,h}-\theta^+_{n,1})-V_{n,h}(\Delta\theta_h-\Delta\hat{\theta}_h)\sin(\theta_{n,h}-\theta^+_{n,1})\Big] \tag{11a}$$

$$\frac{d(\Delta\hat{\theta}^+_1)}{dt}\approx\Delta\hat{\omega}+k_1\left[(\Delta\theta^+_1-\Delta\hat{\theta}^+_1)+\frac{\Delta V_h-\Delta\hat{V}_h}{V^+_{n,1}}\sin(\theta_{n,h}-\theta^+_{n,1})+\frac{V_{n,h}}{V^+_{n,1}}(\Delta\theta_h-\Delta\hat{\theta}_h)\cos(\theta_{n,h}-\theta^+_{n,1})\right] \tag{11b}$$

$$\frac{d(\Delta\hat{V}_h)}{dt}\approx k_h\Big[(\Delta V_h-\Delta\hat{V}_h)+(\Delta V^+_1-\Delta\hat{V}^+_1)\cos(\theta_{n,h}-\theta^+_{n,1})+V^+_{n,1}(\Delta\theta^+_1-\Delta\hat{\theta}^+_1)\sin(\theta_{n,h}-\theta^+_{n,1})\Big] \tag{11c}$$

$$\frac{d(\Delta\hat{\theta}_h)}{dt}\approx h\Delta\hat{\omega}+k_h\left[(\Delta\theta_h-\Delta\hat{\theta}_h)-\frac{\Delta V^+_1-\Delta\hat{V}^+_1}{V_{n,h}}\sin(\theta_{n,h}-\theta^+_{n,1})+\frac{V^+_{n,1}}{V_{n,h}}(\Delta\theta^+_1-\Delta\hat{\theta}^+_1)\cos(\theta_{n,h}-\theta^+_{n,1})\right] \tag{11d}$$

$$\frac{d(\Delta\hat{\omega})}{dt}\approx\lambda\left[(\Delta\theta^+_1-\Delta\hat{\theta}^+_1)+\frac{\Delta V_h-\Delta\hat{V}_h}{V^+_{n,1}}\sin(\theta_{n,h}-\theta^+_{n,1})+\frac{V_{n,h}}{V^+_{n,1}}(\Delta\theta_h-\Delta\hat{\theta}_h)\cos(\theta_{n,h}-\theta^+_{n,1})\right] \tag{11e}$$

$R = k_h/k_1$ (i.e., $R = 0.25$, $R = 0.75$, and $R = 1.5$) can be observed in Fig. 7. Similar results can be obtained for the case of $h = +7$. To save space, they are not presented here. From Fig. 7, the following observations can be made.

1) The stability region of the DROGI-FLL reduces with increasing the ratio R. This result was expected as a higher value for R is corresponding to a more strong dynamic interaction between different frequency components in the DROGI-FLL. This fact may also be deduced from the open-loop HTF in (14).
2) For a given value of R, increasing Γ reduces the maximum allowable k_1 for ensuring stability. Recall that $\Gamma = \lambda/k_1$.

To support the aforementioned observations, the accuracy of the theoretically predicted stability border for the DROGI-FLL in Fig. 7(b) is examined numerically. To this end, the actual DROGI-FLL (see Fig. 1) is digitally implemented in MATLAB/Simulink, and the maximum allowable value of k_1 for ensuring its stability for different values of Γ is determined. The method suggested in [34, Fig. 7] is used for the discretization of the DROGI-FLL. To take into account the effect of the sampling frequency on these results, the simulation studies are carried out with different sampling frequencies. Fig. 8 shows the obtained results. It is observed that there are some rather small errors between the theoretically predicted (solid line) and numerically obtained results when the sampling frequency is 10 kHz. Note that this difference is mainly because of the error caused by the discretization of the DROGI-FLL. By increasing the sampling frequency, as expected, this error is considerably reduced. At

$$
\underbrace{\begin{bmatrix}
\vdots \\
\Delta\hat{V}_1^+(s-j\omega_p) \\
\Delta\hat{\theta}_1^+(s-j\omega_p) \\
\Delta\hat{V}_h(s-j\omega_p) \\
\Delta\hat{\theta}_h(s-j\omega_p) \\
\Delta\hat{V}_1^+(s) \\
\Delta\hat{\theta}_1^+(s) \\
\Delta\hat{V}_h(s) \\
\Delta\hat{\theta}_h(s) \\
\Delta\hat{V}_1^+(s+j\omega_p) \\
\Delta\hat{\theta}_1^+(s+j\omega_p) \\
\Delta\hat{V}_h(s+j\omega_p) \\
\Delta\hat{\theta}_h(s+j\omega_p) \\
\vdots
\end{bmatrix}}_{Y} = k_1 \begin{bmatrix}
\ddots & \vdots & \vdots & \vdots & \vdots & \vdots & \vdots \\
\cdots & \frac{1}{s-j\omega_p} & 0 & 0 & 0 & 0 & 0 \\
\cdots & 0 & \frac{(s-j\omega_p)+\Gamma}{(s-j\omega_p)^2} & 0 & 0 & 0 & 0 \\
\cdots & 0 & 0 & \frac{R}{(s-j\omega_p)} & 0 & \frac{R}{2(s-j\omega_p)} & j\frac{RV_{n,1}^+}{2(s-j\omega_p)} \\
\cdots & 0 & \frac{h\Gamma}{(s-j\omega_p)^2} & 0 & \frac{R}{(s-j\omega_p)} & -\frac{jR}{2V_{n,h}(s-j\omega_p)} & \frac{V_{n,1}^+R}{2V_{n,h}(s-j\omega_p)} \\
\cdots & 0 & 0 & \frac{1}{2s} & \frac{jV_{n,h}}{2s} & \frac{1}{s} & 0 \\
\cdots & 0 & 0 & -j\frac{s+\Gamma}{2V_{n,1}^+s^2} & \frac{V_{n,h}(s+\Gamma)}{2V_{n,1}^+s^2} & 0 & \frac{s+\Gamma}{s^2} \\
\cdots & \frac{R}{2s} & -j\frac{RV_{n,1}^+}{2s} & 0 & 0 & 0 & 0 \\
\cdots & \frac{jR}{2V_{n,h}s} & \frac{V_{n,1}^+R}{2V_{n,h}s} & -j\frac{h\Gamma}{2V_{n,1}^+s^2} & \frac{hV_{n,h}\Gamma}{2V_{n,1}^+s^2} & 0 & \frac{h\Gamma}{s^2} \\
\cdots & 0 & 0 & 0 & 0 & 0 & 0 \\
\cdots & 0 & 0 & 0 & 0 & 0 & 0 \\
\cdots & 0 & 0 & 0 & 0 & \frac{R}{2(s+j\omega_p)} & -j\frac{RV_{n,1}^+}{2(s+j\omega_p)} \\
\cdots & 0 & 0 & 0 & 0 & \frac{jR}{2V_{n,h}(s+j\omega_p)} & \frac{V_{n,1}^+R}{2V_{n,h}(s+j\omega_p)} \\
 & \vdots & \vdots & \vdots & \vdots & \vdots & \vdots
\end{bmatrix}
$$

$$
\begin{bmatrix}
\vdots & \vdots & \vdots & \vdots & \vdots & \vdots & \\
\frac{1}{2(s-j\omega_p)} & \frac{-jV_{n,h}}{2(s-j\omega_p)} & 0 & 0 & 0 & 0 & \cdots \\
j\frac{(s-j\omega_p)+\Gamma}{2V_{n,1}^+(s-j\omega_p)^2} & \frac{V_{n,h}((s-j\omega_p)+\Gamma)}{2V_{n,1}^+(s-j\omega_p)^2} & 0 & 0 & 0 & 0 & \cdots \\
0 & 0 & 0 & 0 & 0 & 0 & \cdots \\
j\frac{h\Gamma}{2V_{n,1}^+(s-j\omega_p)^2} & \frac{hV_{n,h}\Gamma}{2V_{n,1}^+(s-j\omega_p)^2} & 0 & 0 & 0 & 0 & \cdots \\
0 & 0 & 0 & 0 & \frac{1}{2s} & \frac{-jV_{n,h}}{2s} & \cdots \\
0 & 0 & 0 & 0 & j\frac{s+\Gamma}{2V_{n,1}^+s^2} & \frac{V_{n,h}(s+\Gamma)}{2V_{n,1}^+s^2} & \cdots \\
\frac{R}{s} & 0 & \frac{R}{2s} & j\frac{RV_{n,1}^+}{2s} & 0 & 0 & \cdots \\
0 & \frac{R}{s} & -\frac{jR}{2V_{n,h}s} & \frac{V_{n,1}^+R}{2V_{n,h}s} & j\frac{h\Gamma}{2V_{n,1}^+s^2} & \frac{hV_{n,h}\Gamma}{2V_{n,1}^+s^2} & \cdots \\
\frac{1}{2(s+j\omega_p)} & \frac{jV_{n,h}}{2(s+j\omega_p)} & \frac{1}{(s+j\omega_p)} & 0 & 0 & 0 & \cdots \\
-j\frac{(s+j\omega_p)+\Gamma}{2V_{n,1}^+(s+j\omega_p)^2} & \frac{V_{n,h}((s+j\omega_p)+\Gamma)}{2V_{n,1}^+(s+j\omega_p)^2} & 0 & \frac{(s+j\omega_p)+\Gamma}{(s+j\omega_p)^2} & 0 & 0 & \cdots \\
0 & 0 & 0 & 0 & \frac{R}{(s+j\omega_p)} & 0 & \cdots \\
-j\frac{h\Gamma}{2V_{n,1}^+(s+j\omega_p)^2} & \frac{hV_{n,h}\Gamma}{2V_{n,1}^+(s+j\omega_p)^2} & 0 & \frac{h\Gamma}{(s+j\omega_p)^2} & 0 & \frac{R}{(s+j\omega_p)} & \cdots \\
\vdots & \vdots & \vdots & \vdots & \vdots & \vdots & \ddots
\end{bmatrix}
\underbrace{\begin{bmatrix}
\vdots \\
\Delta V_{e,1}^+(s-j\omega_p) \\
\Delta\theta_{e,1}^+(s-j\omega_p) \\
\Delta V_{e,h}(s-j\omega_p) \\
\Delta\theta_{e,h}(s-j\omega_p) \\
\Delta V_{e,1}^+(s) \\
\Delta\theta_{e,1}^+(s) \\
\Delta V_{e,h}(s) \\
\Delta\theta_{e,h}(s) \\
\Delta V_{e,1}^+(s+j\omega_p) \\
\Delta\theta_{e,1}^+(s+j\omega_p) \\
\Delta V_{e,h}(s+j\omega_p) \\
\Delta\theta_{e,h}(s+j\omega_p) \\
\vdots
\end{bmatrix}}_{E} \tag{14}
$$

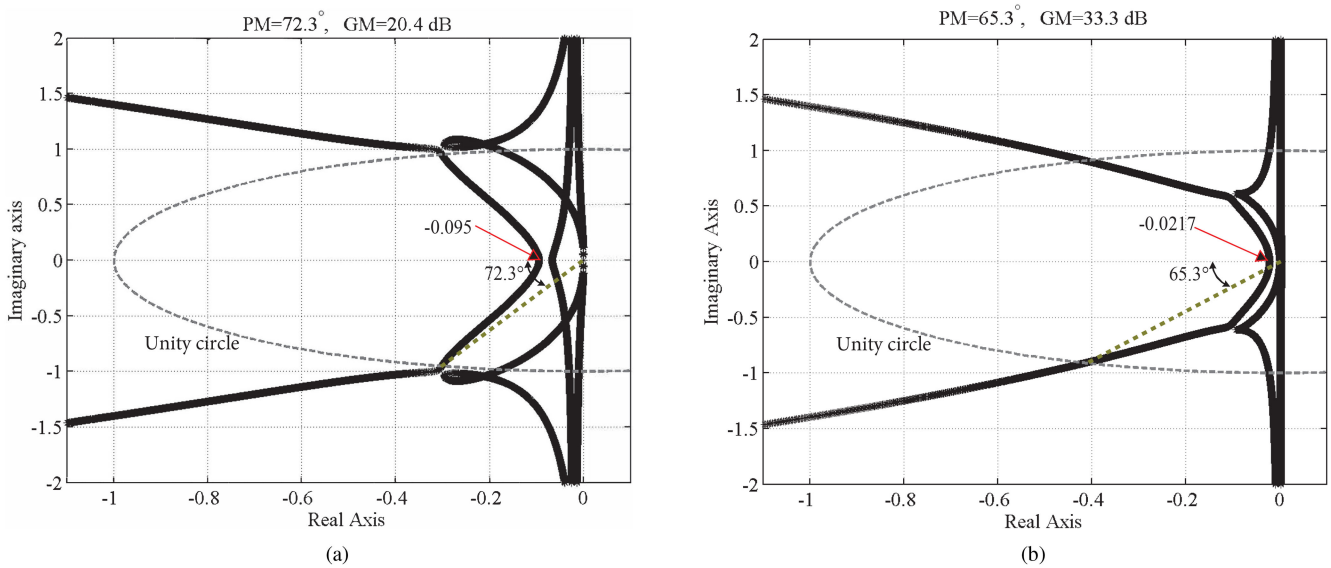

Fig. 6. Open-loop LTP Nyquist plots of the DROGI-FLL. (a) Case 1 ($h = -1$). (b) Case 2 ($h = +7$). In both cases, the DROGI-FLL has the same set of control parameters, as summarized in Table I, i.e., $k_1 = k_h = 177$ and $\lambda = 16\,000$. The nominal amplitudes are $V_{n,1}^{+} = 1$ p.u. and $V_{n,h} = 0.2$ p.u. The initial phase $\delta_h = 0$ is assumed.

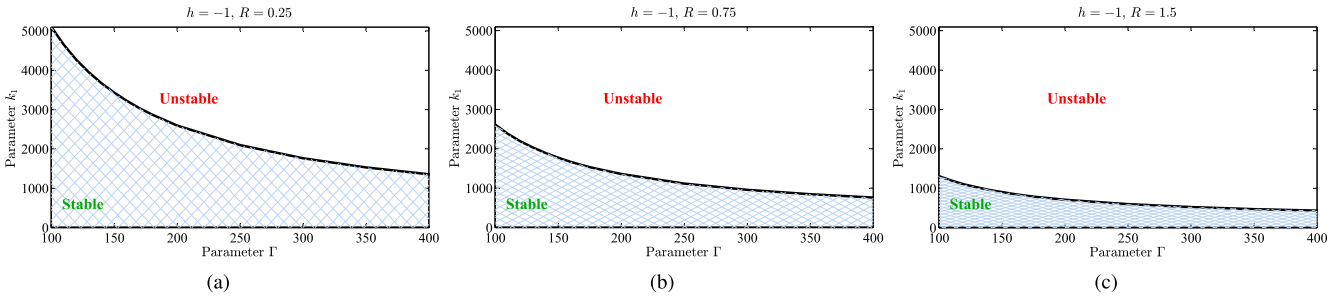

Fig. 7. Stability region of the DROGI-FLL for $h = -1$ and different values of R. (a) $R = 0.25$. (b) $R = 0.75$. (c) $R = 1.5$. The nominal amplitudes are $V_{n,1}^{+} = 1$ p.u. and $V_{n,1}^{-} = 0.2$ p.u. The initial phase $\delta_h = 0$ is assumed.

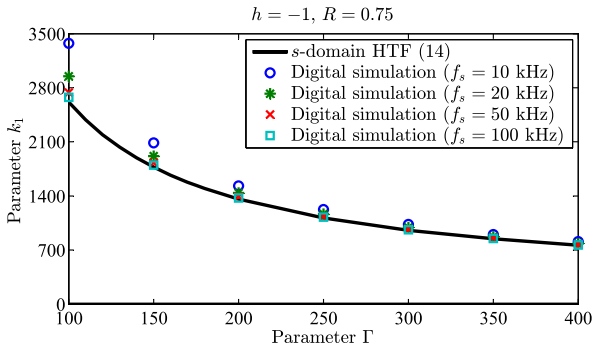

Fig. 8. Comparison of the theoretically predicted stability border for the DROGI-FLL in Fig. 7(b) with the numerically determined ones. The condition of obtaining the results is the same as Fig. 7(b). f_s is the sampling frequency in the simulation studies.

$f_s = 50$ kHz, for example, the theoretical and simulation results are almost converged.

It is worth mentioning at the end of this section that the modeling procedure and stability analysis presented for the case of the DROGI-FLL may be extended to the case of multi-ROGI-FLL. The multi-ROGI-FLL, as mentioned before, includes several ROGIs centered at the fundamental positive and negative frequencies and one or more harmonic frequencies. This issue will be further investigated in future works.

III. Dual Second-Order Generalized Integrator Based FLL

A. Overview

The DSOGI-FLL [37], which is shown in Fig. 9, is the second case study in this article.[4] It is one of the most popular time-domain signal decomposition algorithms for unbalanced grid scenarios, which can be easily extended to take into account

[4]This representation of the DSOGI-FLL has a small difference compared to the original one, which is shown in [37, Fig. 10]. In the original structure, the input signal of the integrator of the FLL is multiplied by the estimated frequency $\hat{\omega}$. This multiplication is neglected in this article.

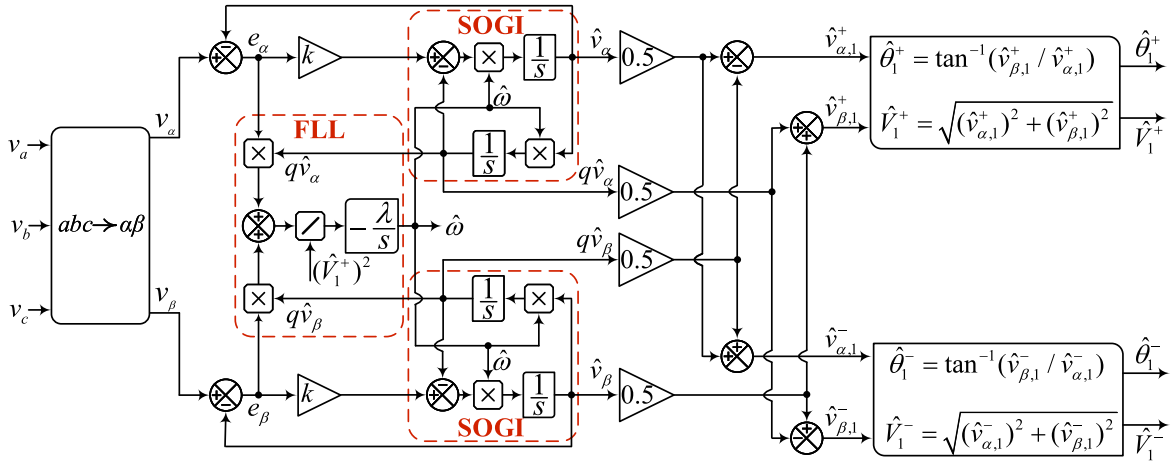

Fig. 9. DSOGI-FLL. k and λ are the control parameters. $\hat{v}_\alpha$ and $\hat{v}_\beta$ are estimations of the fundamental component of v_α and v_β, respectively. $q\hat{v}_\alpha$ and $q\hat{v}_\beta$ are 90° phase-lagged versions of $\hat{v}_\alpha$ and $\hat{v}_\beta$, respectively. $\hat{v}_{\alpha,1}^+$ and $\hat{v}_{\beta,1}^+$ ($\hat{v}_{\alpha,1}^-$ and $\hat{v}_{\beta,1}^-$) are estimations of the FFPS (FFNS) components of the grid voltage in the $\alpha\beta$ frame. $\hat{\theta}_1^+$ and $\hat{V}_1^+$ ($\hat{\theta}_1^-$ and $\hat{V}_1^-$) are the estimation of the phase angle and amplitude of the FFPS (FFNS) component of the grid voltage. $\hat{\omega}$ is an estimation of the fundamental angular frequency of the grid voltage.

the presence of harmonics [19].[5] In what follows, the operating principle of the DSOGI-FLL is explained.

Let us neglect the presence of harmonics in the DSOGI-FLL input and consider $\boldsymbol{v}_{abc}$ as a set of unbalanced signals as follows:

$$\boldsymbol{v}_{abc} = \boldsymbol{v}_{abc,1}^{+} + \boldsymbol{v}_{abc,1}^{-} + \boldsymbol{v}_{abc,1}^{z}. \tag{15}$$

In the aforementioned equation, $\boldsymbol{v}_{abc,1}^{+}$, $\boldsymbol{v}_{abc,1}^{-}$, and $\boldsymbol{v}_{abc,1}^{z}$ are the fundamental positive, negative, and zero sequence components, which can be determined by applying Lyon's transformation $\boldsymbol{T}^{+}$, $\boldsymbol{T}^{-}$, and $\boldsymbol{T}^{z}$ to $\boldsymbol{v}_{abc}$, respectively [37]. Applying Clarke's transformation $\boldsymbol{T}_{\alpha\beta}$ to (15) results in

$$\overbrace{\boldsymbol{T}_{\alpha\beta}\boldsymbol{v}_{abc}}^{\boldsymbol{v}_{\alpha\beta}} = \overbrace{\boldsymbol{T}_{\alpha\beta}\boldsymbol{v}_{abc,1}^{+}}^{\boldsymbol{v}_{\alpha\beta,1}^{+}} + \overbrace{\boldsymbol{T}_{\alpha\beta}\boldsymbol{v}_{abc,1}^{-}}^{\boldsymbol{v}_{\alpha\beta,1}^{-}} + \overbrace{\boldsymbol{T}_{\alpha\beta}\boldsymbol{v}_{abc,1}^{z}}^{0} \tag{16}$$

where

$$\boldsymbol{v}_{\alpha\beta,1}^{+} = \boldsymbol{T}_{\alpha\beta}\boldsymbol{v}_{abc,1}^{+} = \boldsymbol{T}_{\alpha\beta}\boldsymbol{T}^{+}\boldsymbol{v}_{abc} = \boldsymbol{T}_{\alpha\beta}\boldsymbol{T}^{+}\text{pinv}(\boldsymbol{T}_{\alpha\beta})\boldsymbol{v}_{\alpha\beta}$$
$$= \frac{1}{2}\begin{pmatrix} 1 & -q \\ q & 1 \end{pmatrix}\boldsymbol{v}_{\alpha\beta} \tag{17a}$$

$$\boldsymbol{v}_{\alpha\beta,1}^{-} = \boldsymbol{T}_{\alpha\beta}\boldsymbol{v}_{abc,1}^{-} = \boldsymbol{T}_{\alpha\beta}\boldsymbol{T}^{-}\boldsymbol{v}_{abc} = \boldsymbol{T}_{\alpha\beta}\boldsymbol{T}^{-}\text{pinv}(\boldsymbol{T}_{\alpha\beta})\boldsymbol{v}_{\alpha\beta}$$
$$= \frac{1}{2}\begin{pmatrix} 1 & q \\ -q & 1 \end{pmatrix}\boldsymbol{v}_{\alpha\beta}. \tag{17b}$$

In (17), pinv$(\cdot)$ denotes the pseudoinverse, and $q = e^{-j\pi/2}$, which means that the $-90°$ phase-shifted version of the signals v_α and v_β is required for extracting the FFPS and FFNS components of the grid voltage in the $\alpha\beta$ frame [37]. The DSOGI-FLL, as shown in Fig. 9, uses two SOGIs[6] in unity feedback loops for this purpose. Such configuration provides the filtered versions of the $\alpha\beta$-axis grid voltage signals and their $-90°$ phase-shifted version. The center frequency of SOGIs is adapted to frequency changes using an FLL. The governing differential equations of this FLL can be obtained using the gradient descent method.

B. Harmonic Modeling

The harmonic modeling of the DSOGI-FLL can be carried out by following a similar mathematical procedure as that presented for the case of the DROGI-FLL. However, to save space here, a mixed intuitive/mathematical procedure is presented. The intuitive part of this procedure is based on finding a relationship between the DSOGI-FLL and DROGI-FLL.

First, let us neglect the dynamics of the FLL in Fig. 9, and consider the center frequency of the SOGIs constant. In this case, the characteristic transfer functions of the DSOGI-FLL can be obtained as

$$\frac{\hat{v}_{\alpha,1}^{+}(s) + j\hat{v}_{\beta,1}^{+}(s)}{v_\alpha(s) + jv_\beta(s)} = \frac{0.5k\hat{\omega}(s + j\hat{\omega})}{s^2 + k\hat{\omega}s + \hat{\omega}^2} \tag{18a}$$

$$\frac{\hat{v}_{\alpha,1}^{-}(s) + j\hat{v}_{\beta,1}^{-}(s)}{v_\alpha(s) + jv_\beta(s)} = \frac{0.5k\hat{\omega}(s - j\hat{\omega})}{s^2 + k\hat{\omega}s + \hat{\omega}^2}. \tag{18b}$$

Considering the same assumption in the DROGI-FLL (see Fig. 1) gives

$$\frac{\hat{v}_{\alpha,1}^{+}(s) + j\hat{v}_{\beta,1}^{+}(s)}{v_\alpha(s) + jv_\beta(s)} = \frac{k_1(s - jh\hat{\omega})}{(s - j\hat{\omega})(s - jh\hat{\omega} + k_h) + k_1(s - jh\hat{\omega})} \tag{19a}$$

$$\frac{\hat{v}_{\alpha,h}(s) + j\hat{v}_{\beta,h}(s)}{v_\alpha(s) + jv_\beta(s)} = \frac{k_h(s - j\hat{\omega})}{(s - jh\hat{\omega})(s - j\hat{\omega} + k_1) + k_h(s - j\hat{\omega})}. \tag{19b}$$

[5] Taking into account a single harmonic requires two additional SOGIs (tuned to the concerned harmonic frequency) in parallel with the main SOGIs. In this case, it should be called the multi-SOGI-FLL.

[6] A SOGI is a resonant controller with two complex conjugate poles at the concerned frequency (here, the fundamental frequency).

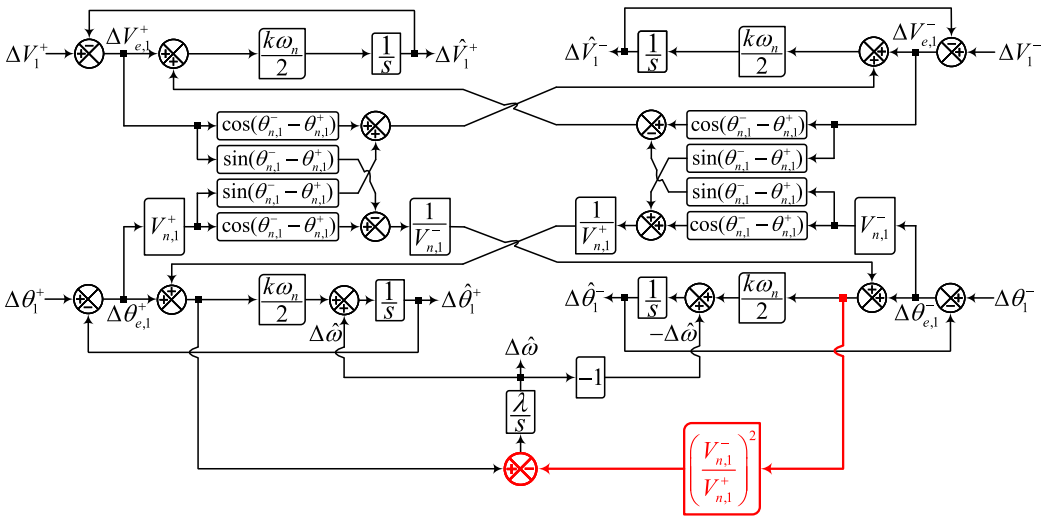

Fig. 10. Harmonic model (LTP model) of the DSOGI-FLL.

It can be shown that (18a) and (19a) are the same transfer functions if $h=-1$ and $k_1=k_h=0.5k\hat{\omega}$.[7] The same goes for the case of (18b) and (19b). It implies that the linearized equations (11a)–(11d), which were obtained for the DROGI-FLL, are also valid for the case of the DSOGI-FLL. We just need to consider $h=-1$ and $k_1=k_h=0.5\ k\omega_n$ in these equations.

The FLL of the DSOGI-FLL, however, is a bit different from that of DROGI-FLL. Therefore, we need to perform the linearization process for it again.

From Fig. 9, the time derivative of the estimated frequency in the DSOGI-FLL can be expressed as

$$\begin{aligned}\frac{d\hat{\omega}}{dt} &= -\frac{\lambda}{\left(\hat{V}_1^+\right)^2}\left[(v_\alpha-\hat{v}_\alpha)q\hat{v}_\alpha+(v_\beta-\hat{v}_\beta)q\hat{v}_\beta\right]\\ &= \frac{\lambda}{\left(\hat{V}_1^+\right)^2}\Big[(v_\beta-\hat{v}_{\beta,1}^+-\hat{v}_{\beta,1}^-)(\hat{v}_{\alpha,1}^+-\hat{v}_{\alpha,1}^-)\\ &\qquad -(v_\alpha-\hat{v}_{\alpha,1}^+-\hat{v}_{\alpha,1}^-)(\hat{v}_{\beta,1}^+-\hat{v}_{\beta,1}^-)\Big]\end{aligned} \tag{20}$$

where

$$\begin{pmatrix}v_\alpha\\ v_\beta\end{pmatrix}=\begin{pmatrix}V_1^+\cos(\theta_1^+)\\ V_1^+\sin(\theta_1^+)\end{pmatrix}+\begin{pmatrix}V_1^-\cos(\theta_1^-)\\ V_1^-\sin(\theta_1^-)\end{pmatrix} \tag{21a}$$

$$\begin{pmatrix}\hat{v}_{\alpha,1}^+\\ \hat{v}_{\beta,1}^+\end{pmatrix}=\begin{pmatrix}\hat{V}_1^+\cos(\hat{\theta}_1^+)\\ \hat{V}_1^+\sin(\hat{\theta}_1^+)\end{pmatrix} \tag{21b}$$

$$\begin{pmatrix}\hat{v}_{\alpha,1}^-\\ \hat{v}_{\beta,1}^-\end{pmatrix}=\begin{pmatrix}\hat{V}_1^-\cos(\hat{\theta}_1^-)\\ \hat{V}_1^-\sin(\hat{\theta}_1^-)\end{pmatrix} \tag{21c}$$

and

$$\begin{aligned}&V_1^+=V_{n,1}^+\angle\theta_1^+ + \Delta V_1^+\angle\theta_1^+, && \hat{V}_1^+=V_{n,1}^+\angle\theta_1^+ + \Delta\hat{V}_1^+\angle\hat{\theta}_1^+\\ &\theta_1^+=\theta_{n,1}^+ + \Delta\theta_1^+, && \hat{\theta}_1^+=\theta_{n,1}^+ + \Delta\hat{\theta}_1^+\\ &V_1^-=V_{n,1}^-\angle\theta_1^- + \Delta V_1^-\angle\theta_1^-, && \hat{V}_1^-=V_{n,1}^-\angle\theta_1^- + \Delta\hat{V}_1^-\angle\hat{\theta}_1^-\\ &\theta_1^-=\theta_{n,1}^- + \Delta\theta_1^-, && \hat{\theta}_1^-=\theta_{n,1}^- + \Delta\hat{\theta}_1^-\\ &\omega=\omega_n+\Delta\omega, && \hat{\omega}=\omega_n+\Delta\hat{\omega}.\end{aligned} \tag{22}$$

By substituting (21) into (20), applying trigonometric identities, considering definitions made in (22), and following a similar linearization procedure as in (11), (20) can be linearized as (23) shown at the bottom of this page. Considering this equation and the previous discussions about the relationship of the DSOGI-FLL and DROGI-FLL, the harmonic model of the DSOGI-FLL may be obtained, as depicted in Fig. 10. Notice that this model has a difference (an additional loop, which is highlighted with red color) compared to that of the DROGI-FLL. This additional loop, however, does not mean that the DSOGI-FLL has very different transient behavior compared to the DROGI-FLL, at least from the small-signal point of view. The reason is that the gain $(V_{n,1}^-/V_{n,1}^+)^2$ in the highlighted loop in Fig. 10 is a small value in most practical cases.

C. Model Verification

To evaluate the accuracy of the obtained harmonic model for the DSOGI-FLL, the same conditions and tests as in Fig. 4 are

[7] As k_1 and k_h are constants and $\hat{\omega}$ is a variable in practice, $k_1=k_h=0.5\ k\omega_n$ needs to be considered in practice.

$$\begin{aligned}\frac{d(\Delta\hat{\omega})}{dt} \approx{}& \lambda\left[(\Delta\theta_1^+-\Delta\hat{\theta}_1^+)+\frac{\Delta V_1^- - \Delta\hat{V}_1^-}{V_{n,1}^+}\sin(\theta_{n,1}^- - \theta_{n,1}^+)+\frac{V_{n,1}^-}{V_{n,1}^+}(\Delta\theta_1^- - \Delta\hat{\theta}_1^-)\cos(\theta_{n,1}^- - \theta_{n,1}^+)\right]\\ &-\lambda\left(\frac{V_{n,1}^-}{V_{n,1}^+}\right)^2\left[(\Delta\theta_1^- - \Delta\hat{\theta}_1^-)-\frac{\Delta V_1^+ - \Delta\hat{V}_1^+}{V_{n,1}^-}\sin(\theta_{n,1}^- - \theta_{n,1}^+)+\frac{V_{n,1}^+}{V_{n,1}^-}(\Delta\theta_1^+ - \Delta\hat{\theta}_1^+)\cos(\theta_{n,1}^- - \theta_{n,1}^+)\right]\end{aligned} \tag{23}$$

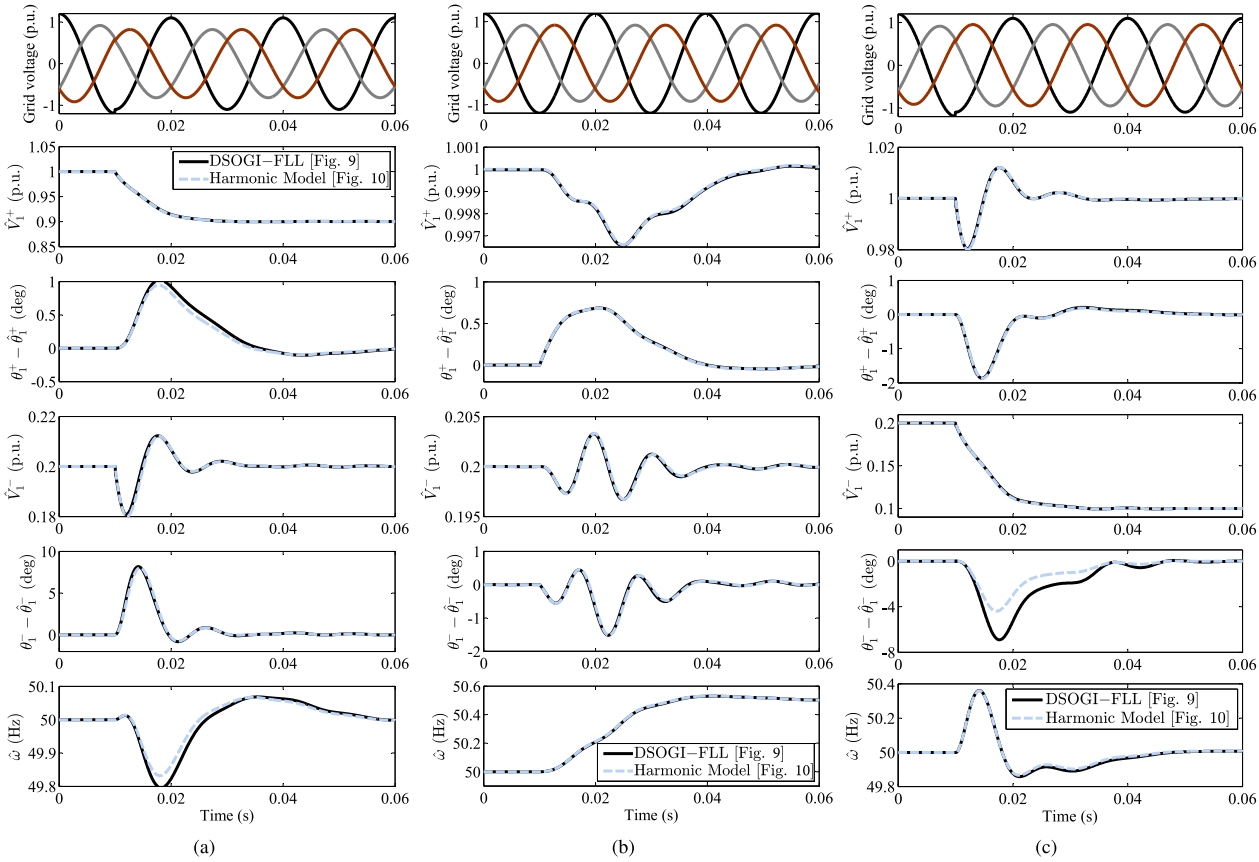

Fig. 11. Model verification of the DSOGI-FLL. (a) Test A. (b) Test B. (c) Test C.

considered. The control parameters of the DSOGI-FLL can be found in Table I. Fig. 11 shows the results of the evaluation. It is observed that the LTP model offers high accuracy in predicting the DSOGI-FLL dynamics in estimating the fundamental positive- and negative sequence parameters of the grid voltage and the dynamic interaction between their estimation loops.

In a similar manner as in Section II-C.2, the open-loop HTF of the DSOGI-FLL can be obtained and its stability can be investigated. Here, to save space, this analysis is not presented.

IV. Modified UTSP

A. Overview

The UTSP is the parallel connection of three PLLs, which work in a collaborative manner and extract the magnitude, phase angle, and frequency of the fundamental-frequency positive-, negative-, and zero sequence components and their sinusoidal waveforms (see [17, Fig. 1]). In [25], removing the zero sequence estimation loop of the UTSP is proposed. In this way, the estimation loops can be implemented in the two-phase format, which results in a noticeable reduction in the implementation complexity and computational burden. Simplifying the frequency estimation logic and introducing amplitude normalization are other contributions in [25]. Fig. 12 shows the final product, which is referred to as the modified UTSP.

The modified UTSP includes two SRF-PLLs, which work collaboratively. Note that only the upper SRF-PLL (i.e., the SRF-PLL responsible for extracting the FFPS component) estimates the grid angular frequency, and the lower one only uses this signal. Note also that the modified UTSP can be easily extended to take into account the presence of harmonic components by adding additional SRF-PLLs tuned to harmonic frequencies.

B. Harmonic Modeling

The harmonic modeling of the modified UTSP can be carried out by following a similar procedure as in Section II-B. However, to save space, an intuitive way is presented here.

In Fig. 12, the signals e_d^+, e_q^+, e_d^-, and e_q^- can be expressed as

$$\begin{bmatrix} e_d^+ \\ e_q^+ \end{bmatrix} = \begin{bmatrix} \cos(\hat{\theta}_1^+) & \sin(\hat{\theta}_1^+) \\ -\sin(\hat{\theta}_1^+) & \cos(\hat{\theta}_1^+) \end{bmatrix} \begin{bmatrix} e_\alpha \\ e_\beta \end{bmatrix} = \frac{1}{\hat{V}_1^+} \begin{bmatrix} \hat{v}_{\alpha,1}^+ & \hat{v}_{\beta,1}^+ \\ -\hat{v}_{\beta,1}^+ & \hat{v}_{\alpha,1}^+ \end{bmatrix} \begin{bmatrix} e_\alpha \\ e_\beta \end{bmatrix} \tag{24a}$$

$$\begin{bmatrix} e_d^- \\ e_q^- \end{bmatrix} = \begin{bmatrix} \cos(\hat{\theta}_1^-) & \sin(\hat{\theta}_1^-) \\ -\sin(\hat{\theta}_1^-) & \cos(\hat{\theta}_1^-) \end{bmatrix} \begin{bmatrix} e_\alpha \\ e_\beta \end{bmatrix} = \frac{1}{\hat{V}_1^-} \begin{bmatrix} \hat{v}_{\alpha,1}^- & \hat{v}_{\beta,1}^- \\ -\hat{v}_{\beta,1}^- & \hat{v}_{\alpha,1}^- \end{bmatrix} \begin{bmatrix} e_\alpha \\ e_\beta \end{bmatrix} \tag{24b}$$

where $e_\alpha = v_\alpha - \hat{v}_{\alpha,1}^+ - \hat{v}_{\alpha,1}^-$ and $e_\beta = v_\beta - \hat{v}_{\beta,1}^+ - \hat{v}_{\beta,1}^-$.

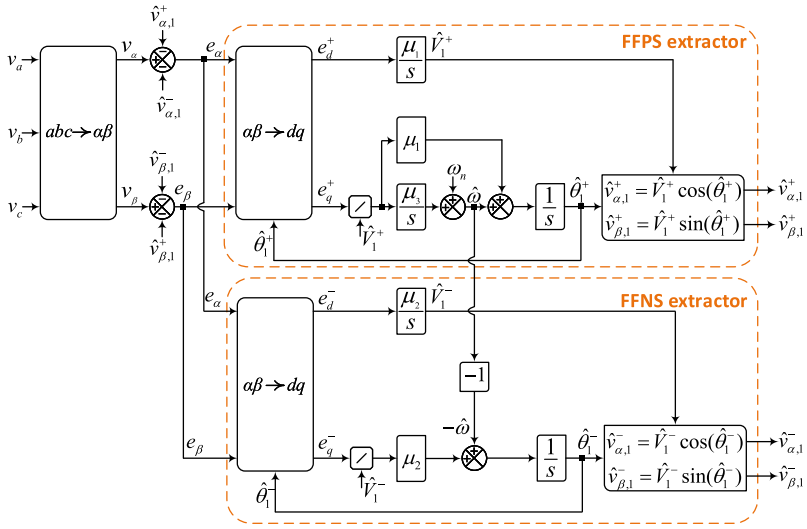

Fig. 12. Modified UTSP. μ_1, μ_2, and μ_3 are the control parameters.

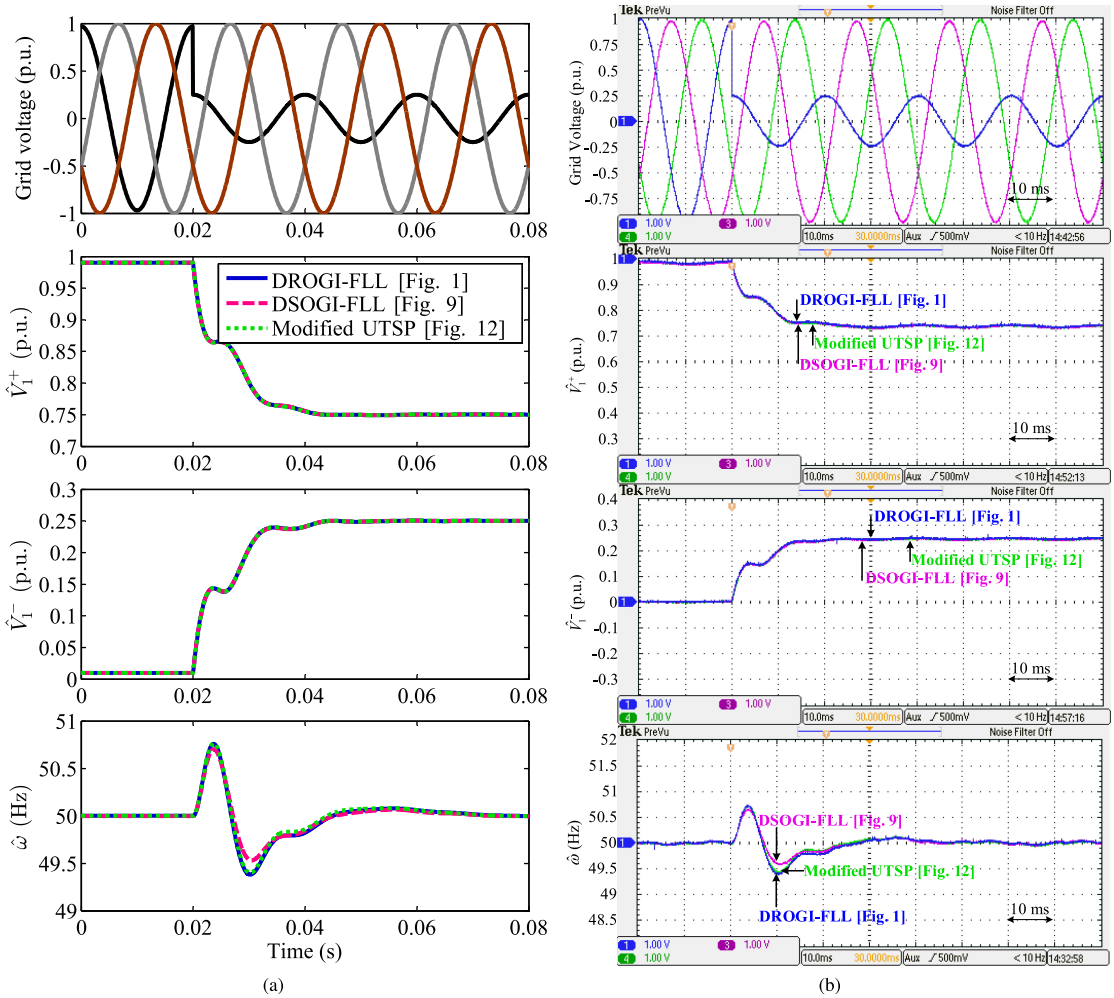

(a) (b)

Fig. 13. Comparison between the DROGI-FLL, DSOGI-FLL, and modified UTSP in response to Test 1. (a) Simulation results. (b) Experimental results.

Using (24) and Fig. 12, the governing nonlinear differential equations of the modified UTSP can be obtained as

$$\frac{d\hat{V}_1^+}{dt} = \mu_1 e_d^+ = \frac{\mu_1}{\hat{V}_1^+}\left[\hat{v}_{\alpha,1}^+ e_\alpha + \hat{v}_{\beta,1}^+ e_\beta\right] \tag{25a}$$

$$\frac{d\hat{\theta}_1^+}{dt} = \hat{\omega} + \frac{\mu_1}{\hat{V}_1^+} e_q^+ = \hat{\omega} + \frac{\mu_1}{\left(\hat{V}_1^+\right)^2}\left[-\hat{v}_{\beta,1}^+ e_\alpha + \hat{v}_{\alpha,1}^+ e_\beta\right] \tag{25b}$$

$$\frac{d\hat{V}_1^-}{dt} = \mu_2 e_d^- = \frac{\mu_2}{\hat{V}_1^-}\left[\hat{v}_{\alpha,1}^- e_\alpha + \hat{v}_{\beta,1}^- e_\beta\right] \tag{25c}$$

$$\frac{d\hat{\theta}_1^-}{dt} = -\hat{\omega} + \frac{\mu_2}{\hat{V}_1^-} e_q^- = -\hat{\omega} + \frac{\mu_2}{\left(\hat{V}_1^-\right)^2}\left[-\hat{v}_{\beta,1}^- e_\alpha + \hat{v}_{\alpha,1}^- e_\beta\right] \tag{25d}$$

$$\frac{d\hat{\omega}}{dt} = \frac{\mu_3}{\hat{V}_1^+} e_q^+ = \frac{\mu_3}{\left(\hat{V}_1^+\right)^2}\left[-\hat{v}_{\beta,1}^+ e_\alpha + \hat{v}_{\alpha,1}^+ e_\beta\right]. \tag{25e}$$

It can be observed that these equations are the same as the governing nonlinear differential equations of the DROGI-FLL [see (9)] if $h = -1$, $k_1 = \mu_1$, $k_h = \mu_2$, and $\lambda = \mu_3$ are considered. Based on this fact, it can be concluded that the DROGI-FLL (for the case of $h = -1$) and the modified UTSP are mathematically equivalent and, therefore, have the same harmonic model (see Fig. 2). It can also be concluded that the harmonic stability analysis performed on the DROGI-FLL is valid for the modified UTSP.

V. Comparison and Discussion

In previous sections, some small-signal tests for evaluating the accuracy of the obtained harmonic models were performed. In this section, the objective is performing some large-signal tests for comparing the performance of the DROGI-FLL ($h = -1$), DSOGI-FLL, and modified UTSP to each other. Both simulation and experimental results are presented. The simulation studies are carried out using MATLAB/Simulink, and experimental ones are conducted using a dSPACE platform (dSPACE 1006) and a grid simulator (Chroma 61845). In both simulation and experimental studies, the sampling frequency is 10 kHz. The control parameters can be found in Table I.

Two tests, as described in the following, are considered here.

1) *Test 1*: The grid voltage undergoes a severe asymmetrical voltage sag. To avoid numerical issues, there is 0.01-p.u. FFNS component in the grid voltage before the voltage dip moment.
2) *Test 2*: The grid voltage, in addition to the FFPS (1 p.u.) and FFNS (0.1 p.u.) components, contains harmonics of order -2, $+4$, -5, $+7$, -11, and $+13$. The magnitude of these harmonics is 0.01, 0.01, 0.05, 0.05, 0.03, and 0.03 p.u., respectively. Suddenly, an exaggeratedly large jump ($+10$-Hz jump) in the grid frequency happens.

The results of these tests are shown in Figs. 13 and 14 . To save space, only the experimental results of Test 1 are presented. As shown, the DROGI-FLL, DSOGI-FLL, and modified UTSP

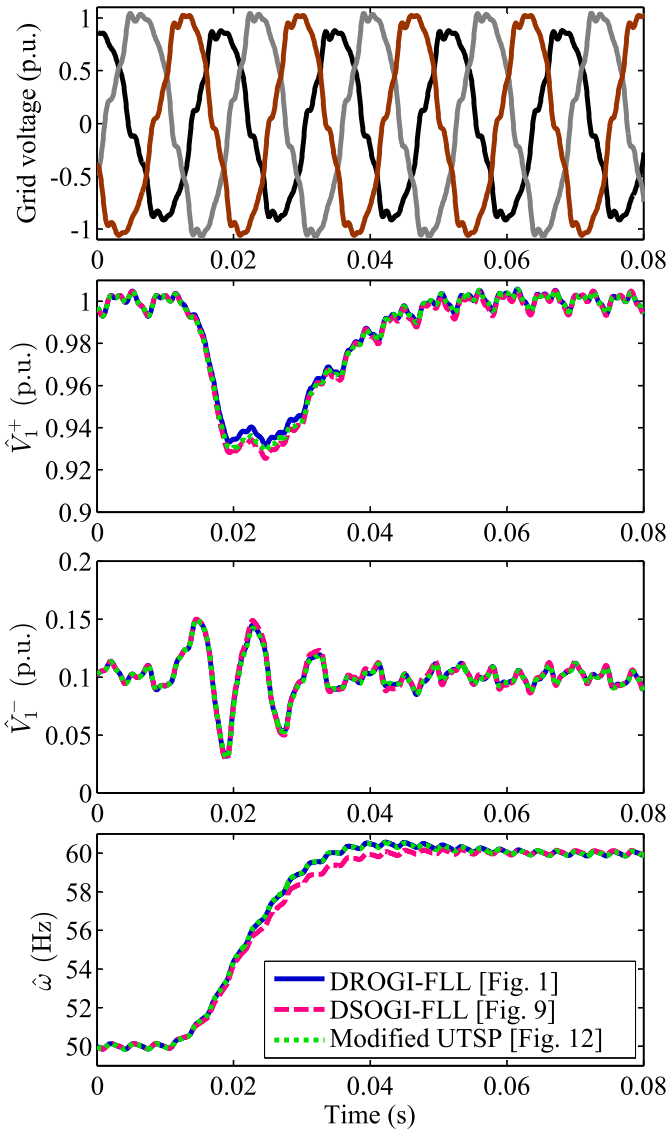

Fig. 14. Comparison between the DROGI-FLL, DSOGI-FLL, and modified UTSP in response to Test 2.

have almost the same transient response and the same level of harmonic filtering capability. These results were expected as we have already proved that the DROGI-FLL and modified UTSP are mathematically equivalent, and demonstrated that the DROGI-FLL and DSOGI-FLL have a close relationship.

An issue that may be interesting to briefly discuss here is the operation of the DROGI-FLL ($h = -1$), DSOGI-FLL, and modified UTSP under a perfectly symmetrical grid scenario (i.e., when the FFNS component of the grid voltage is zero). In such a condition, the signals $\hat{v}_{\alpha,1}^-$ and $\hat{v}_{\beta,1}^-$ (which are the $\alpha\beta$-axis estimation of the grid voltage FFNS component) in the output of the DROGI-FLL and DSOGI-FLL will be equal to zero. Therefore, the DROGI-FLL and DSOGI-FLL have no problem to correctly calculate the amplitude of the FFNS component, i.e., $\hat{V}_1^- = \sqrt{\left(\hat{v}_{\alpha,1}^-\right)^2 + \left(\hat{v}_{\beta,1}^-\right)^2} = 0$. However, in this condition, they cannot determine its phase angle, i.e., $\hat{\theta}_1^- =$

$\tan^{-1}(\hat{v}^-_{\beta,1}/\hat{v}^-_{\alpha,1})$, as the signals $\hat{v}^-_{\alpha,1}$ and $\hat{v}^-_{\beta,1}$ are both equal to zero.

For the case of the modified UTSP, the situation is a bit more involved as the order of operations in this algorithm is different from the DROGI-FLL ($h = -1$) and DSOGI-FLL. Notice that the DROGI-FLL and DSOGI-FLL first extract the grid voltage FFPS and FFNS components in the $\alpha\beta$ frame. These signals are then used for calculating their phase and amplitude. In the modified UTSP, however, the phase and amplitude of the FFPS and FFNS are directly extracted (see Fig. 12). As this process involves regulating the error signals e_q^+ and e_q^- to zero, and there is no FFNS component in the input, the estimation of the FFNS component and its parameters will be lost [38]. That is the reason why in Test 1 (see Fig. 13), a small degree of the grid voltage imbalance was considered before the voltage sag.

It is worth mentioning here that the aforementioned limitation is not a serious issue in practice as the supply voltage has almost always some small degrees of imbalance.

VI. Conclusion

Harmonic modeling and investigation of three-phase time-domain signal decomposition algorithms were the objective of this article. To this end, three case studies were considered. The DROGI-FLL was the first case study. Through a detailed mathematical procedure, which involved obtaining governing nonlinear differential equations of the DROGI-FLL and their harmonic linearization, the harmonic (LTP) model of the DROGI-FLL was obtained and its high accuracy was demonstrated. Using the obtained model, the open-loop HTF of the DROGI-FLL was also obtained and its harmonic stability was investigated. The DSOGI-FLL was the second case study. Through a mixed intuitive/mathematical procedure, the harmonic model of the DSOGI-FLL was obtained, which found to be very similar to that of the DROGI-FLL when $h = -1$ is considered. As the third case study, the modified UTSP was considered. It was demonstrated that the modified UTSP is mathematically equivalent to the DROGI-FLL when $h = -1$ is considered. Based on this fact, it was concluded that they have the same harmonic (LTP) models.

In summary, demonstrating the harmonic modeling and stability assessment of time-domain signal decomposition algorithms, and showing the close mathematical relationship among some state-of-the-art methods in the field are two main contributions of this article. Here, it is worth mentioning that designing really new time-domain signal-decomposition algorithms is very hard, if not impossible. Therefore, researchers should pay careful attention to make sure their final design product is not just an alternative mathematically equivalent representation of available algorithms. Admittedly, even mathematically equivalent systems (depending on their discretization method) may demonstrate different properties in some specific cases (e.g., at low sampling frequencies or in fixed-point implementations with a limited number of bits). These different properties, if any, need to be highlighted by designers.

Acknowledgment

The authors acknowledge with thanks the technical and financial supports of DSR and The Villum Foundation.

References

[1] J. M. Corres, J. Bravo, F. J. Arregui, and I. R. Matias, "Unbalance and harmonics detection in induction motors using an optical fiber sensor," *IEEE Sens. J.*, vol. 6, no. 3, pp. 605–612, Jun. 2006.

[2] J. V. Wijayakulasooriya, G. A. Putrus, and C. H. Ng, "Fast non-recursive extraction of individual harmonics using artificial neural networks," *IEE Proc., Gener. Transmiss. Distrib.*, vol. 152, no. 4, pp. 539–543, Jul. 2005.

[3] P. Rodriguez, A. V. Timbus, R. Teodorescu, M. Liserre, and F. Blaabjerg, "Flexible active power control of distributed power generation systems during grid faults," *IEEE Trans. Ind. Electron.*, vol. 54, no. 5, pp. 2583–2592, Oct. 2007.

[4] P. F. Ribeiro, C. A. Duque, P. M. Ribeiro, and A. S. Cerqueira, *Power Systems Signal Processing for Smart Grids*. Hoboken, NJ, USA: Wiley, 2013.

[5] J. Roldan-Perez, A. Garcia-Cerrada, M. Ochoa-Gimenez, and J. L. Zamora-Macho, "On the power flow limits and control in series-connected custom power devices," *IEEE Trans. Power Electron.*, vol. 31, no. 10, pp. 7328–7338, Oct. 2016.

[6] E. Hossain, M. R. Tur, S. Padmanaban, S. Ay, and I. Khan, "Analysis and mitigation of power quality issues in distributed generation systems using custom power devices," *IEEE Access*, vol. 6, pp. 16816–16833, 2018.

[7] N. Kumar, B. Singh, and B. K. Panigrahi, "LLMLF-based control approach and LPO MPPT technique for improving performance of a multifunctional three-phase two-stage grid integrated PV system," *IEEE Trans. Sustain. Energy*, vol. 11, no. 1, pp. 371–380, Jan. 2020.

[8] V. Narayanan, S. Kewat, and B. Singh, "Solar PV-BES based microgrid system with multifunctional VSC," *IEEE Trans. Ind. Appl.*, vol. 56, no. 3, pp. 2957–2967, May/Jun. 2020.

[9] W. Choi, W. Lee, D. Han, and B. Sarlioglu, "New configuration of multifunctional grid-connected inverter to improve both current-based and voltage-based power quality," *IEEE Trans. Ind. Appl.*, vol. 54, no. 6, pp. 6374–6382, Nov./Dec. 2018.

[10] Y. Han, P. Shen, X. Zhao, and J. M. Guerrero, "Control strategies for islanded microgrid using enhanced hierarchical control structure with multiple current-loop damping schemes," *IEEE Trans. Smart Grid*, vol. 8, no. 3, pp. 1139–1153, May 2017.

[11] *IEEE Standard for Interconnecting Distributed Resources With Electric Power Systems*, IEEE Standard 1547, 2003.

[12] *Technical Regulation 3.2.5 For Wind Power Plants With a Power Output Greater Than 11 kW*, Energinet, Fredericia, Denmark, Tech. Rep. 13/96336-43, 2010.

[13] D. Shin, K. J. Lee, J. P. Lee, D. W. Yoo, and H. J. Kim, "Implementation of fault ride-through techniques of grid-connected inverter for distributed energy resources with adaptive low-pass notch PLL," *IEEE Trans. Power Electron.*, vol. 30, no. 5, pp. 2859–2871, May 2015.

[14] D. Belega, D. Dallet, and D. Slepicka, "Accurate amplitude estimation of harmonic components of incoherently sampled signals in the frequency domain," *IEEE Trans. Instrum. Meas.*, vol. 59, no. 5, pp. 1158–1166, May 2010.

[15] D. Yazdani, A. Bakhshai, G. Joos, and M. Mojiri, "A real-time three-phase selective-harmonic-extraction approach for grid-connected converters," *IEEE Trans. Ind. Electron.*, vol. 56, no. 10, pp. 4097–4106, Oct. 2009.

[16] C. L. Fortescue, "Method of symmetrical co-ordinates applied to the solution of polyphase networks," *Trans. AIEE*, vol. 37, no. 2, pp. 1027–1140, 1918.

[17] M. Karimi-Ghartemani and H. Karimi, "Processing of symmetrical components in time-domain," *IEEE Trans. Power Syst.*, vol. 22, no. 2, pp. 572–579, May 2007.

[18] A. Luna *et al.*, "Grid voltage synchronization for distributed generation systems under grid fault conditions," *IEEE Trans. Ind. Appl.*, vol. 51, no. 4, pp. 3414–3425, Jul. 2015.

[19] P. Rodriguez, A. Luna, I. Candela, R. Mujal, R. Teodorescu, and F. Blaabjerg, "Multiresonant frequency-locked loop for grid synchronization of power converters under distorted grid conditions," *IEEE Trans. Ind. Electron.*, vol. 58, no. 1, pp. 127–138, Jan. 2011.

[20] S. Golestan, J. M. Guerrero, J. C. Vasquez, A. M. Abusorrah, and Y. A. Al-Turki, "Standard SOGI-FLL and its close variants: Precise modeling in LTP framework and determining stability region/robustness metrics," *IEEE Trans. Power Electron.*, vol. 36, no. 1, pp. 409–422, Jan. 2021.

[21] M. Karimi-Ghartemani, M. R. Iravani, and F. Katiraei, "Extraction of signals for harmonics, reactive current and network-unbalance compensation," *IEE Proc., Gener. Transmiss. Distrib.*, vol. 152, no. 1, pp. 137–143, 2005.

[22] X. Guo, W. Wu, and Z. Chen, "Multiple-complex coefficient-filter-based phase-locked loop and synchronization technique for three-phase grid-interfaced converters in distributed utility networks," *IEEE Trans. Ind. Electron.*, vol. 58, no. 4, pp. 1194–1204, Apr. 2011.

[23] W. Li, X. Ruan, C. Bao, D. Pan, and X. Wang, "Grid synchronization systems of three-phase grid-connected power converters: A complex-vector-filter perspective," *IEEE Trans. Ind. Electron.*, vol. 61, no. 4, pp. 1855–1870, Apr. 2014.

[24] S. Golestan and J. M. Guerrero, "Conventional synchronous reference frame phase-locked loop is an adaptive complex filter," *IEEE Trans. Ind. Electron.*, vol. 62, no. 3, pp. 1679–1682, Mar. 2015.

[25] H. Karimi, Y. Seyedi, and M. Karimi-Ghartemani, "A robust and simple phase-locked loop for unbalanced power grid applications," in *Proc. IEEE 28th Int. Symp. Ind. Electron.*, 2019, pp. 29–34.

[26] S. Gomez Jorge, C. A. Busada, and J. A. Solsona, "Frequency adaptive discrete filter for grid synchronization under distorted voltages," *IEEE Trans. Power Electron.*, vol. 27, no. 8, pp. 3584–3594, Aug. 2012.

[27] S. Golestan, J. M. Guerrero, J. C. Vasquez, A. M. Abusorrah, and Y. Al-Turki, "A study on three-phase FLLs," *IEEE Trans. Power Electron.*, vol. 34, no. 1, pp. 213–224, Jan. 2019.

[28] X. Q. Guo and W. Y. Wu, "Simple synchronisation technique for three-phase grid-connected distributed generation systems," *IET Renewable Power Gener.*, vol. 7, no. 1, pp. 55–62, Feb. 2013.

[29] X. Q. Guo, "Frequency-adaptive voltage sequence estimation for grid synchronisation," *Electron. Lett.*, vol. 46, no. 14, pp. 980–982, Jul. 2010.

[30] S. Vazquez, J. A. Sanchez, M. R. Reyes, J. I. Leon, and J. M. Carrasco, "Adaptive vectorial filter for grid synchronization of power converters under unbalanced and/or distorted grid conditions," *IEEE Trans. Ind. Electron.*, vol. 61, no. 3, pp. 1355–1367, Mar. 2014.

[31] Z. Xin, R. Zhao, P. Mattavelli, P. C. Loh, and F. Blaabjerg, "Re-investigation of generalized integrator based filters from a first-order-system perspective," *IEEE Access*, vol. 4, pp. 7131–7144, 2016.

[32] J. Svensson, "Synchronisation methods for grid-connected voltage source converters," *IEE Proc., Gener., Transmiss. Distrib.*, vol. 148, no. 3, pp. 229–235, 2001.

[33] X. Q. Guo and W. Y. Wu, "Improved current regulation of three-phase grid-connected voltage-source inverters for distributed generation systems," *IET Renewable Power Gener.*, vol. 4, no. 2, pp. 101–115, Mar. 2010.

[34] C. A. Busada, S. G. Jorge, A. E. Leon, and J. A. Solsona, "Current controller based on reduced order generalized integrators for distributed generation systems," *IEEE Trans. Ind. Electron.*, vol. 59, no. 7, pp. 2898–2909, Jul. 2012.

[35] S. R. Hall and N. M. Wereley, "Generalized Nyquist stability criterion for linear time periodic systems," in *Proc. Amer. Control Conf.*, May 1990, pp. 1518–1525.

[36] E. Mollerstedt and B. Bernhardsson, "Out of control because of harmonics—An analysis of the harmonic response of an inverter locomotive," *IEEE Control Syst. Mag.*, vol. 20, no. 4, pp. 70–81, Aug. 2000.

[37] P. Rodriguez, A. Luna, R. S. Munoz-Aguilar, I. Etxeberria-Otadui, R. Teodorescu, and F. Blaabjerg, "A stationary reference frame grid synchronization system for three-phase grid-connected power converters under adverse grid conditions," *IEEE Trans. Power Electron.*, vol. 27, no. 1, pp. 99–112, Jan. 2012.

[38] K. S. Narendra and A. M. Annaswamy, "Persistent excitation in adaptive systems," *Int. J. Control*, vol. 45, no. 1, pp. 127–160, 1987.